BIOPHYSICS

Phosphorylation of Doc2 by EphB2 modulates Munc13-mediated SNARE complex assembly and neurotransmitter release

Hong Zhang[1]†, Mengshi Lei[1]†, Yu Zhang[1], Hao Li[2,3], Zhen He[4], Sheng Xie[1], Le Zhu[1], Shen Wang[1], Jianfeng Liu[1], Yan Li[4], Youming Lu[2,3]*, Cong Ma[1,2]*

At the synapse, presynaptic neurotransmitter release is tightly controlled by release machinery, involving the soluble *N*-ethylmaleimide–sensitive factor attachment protein receptor (SNARE) proteins and Munc13. The Ca^{2+} sensor Doc2 cooperates with Munc13 to regulate neurotransmitter release, but the underlying mechanisms remain unclear. In our study, we have characterized the binding mode between Doc2 and Munc13 and found that Doc2 originally occludes Munc13 to inhibit SNARE complex assembly. Moreover, our investigation unveiled that EphB2, a presynaptic adhesion molecule (SAM) with inherent tyrosine kinase functionality, exhibits the capacity to phosphorylate Doc2. This phosphorylation attenuates Doc2 block on Munc13 to promote SNARE complex assembly, which functionally induces spontaneous release and synaptic augmentation. Consistently, application of a Doc2 peptide that interrupts Doc2-Munc13 interplay impairs excitatory synaptic transmission and leads to dysfunction in spatial learning and memory. These data provide evidence that SAMs modulate neurotransmitter release by controlling SNARE complex assembly.

INTRODUCTION

Ca^{2+}-regulated synaptic vesicle exocytosis is a fundamental process for neurotransmitter release and synaptic plasticity. This process requires the fusion of synaptic vesicles with the plasma membrane mediated by the release machinery surrounding the fusion sites (*1*–*3*). As the engine of the release machinery, synaptobrevin-2 (Syb2) on the vesicles and syntaxin-1 (Syx1) and SNAP-25 (SN25) on the plasma membrane assemble into the soluble *N*-ethylmaleimide–sensitive factor attachment protein (SNARE) complex to supply energy for membrane fusion (*4*–*6*). To attain release on demand for diverse neuronal activities, a series of exquisitely spatial and temporal regulations by additional release components need to be imposed on SNARE assembly, enabling SNARE-mediated fusion to happen at the right place, at the correct time, and with the appropriate probability.

In neurons, Munc18-1 and Munc13 are the central SNARE regulatory factors. Munc18-1 clamps Syx1 into a closed conformation that helps their delivery to the plasma membrane but is opposed to Syx1 assembly into the SNARE complex, offering a mechanism for vesicle docking (*7*, *8*). Munc13 enables docked vesicles to mature into the priming process that involves the transition of the Munc18-1/Syx1 complex to the SNARE complex (*9*–*11*). An essential prerequisite for the transition is the opening of Syx1, which is specifically catalyzed by the NF (Asn1128/Phe1131) pocket within the core priming region of Munc13 (the MUN domain) (*12*, *13*). Afterward, the MUN domain in cooperation with Munc18-1 orchestrates SNARE register, pairing, and assembly to accomplish the transition (*14*–*17*). As a master priming factor of release, Munc13 has additional domains capable of modulating its priming activity, thus facilitating diverse forms of release and synaptic plasticity. The C_1-C_2B domain, which binds to diacylglycerol (DAG)/phosphatidylinositol 4,5-bisphosphate (PIP_2)–Ca^{2+} on the plasma membrane (*18*, *19*), and the C_2C domain, which associates with vesicles (*20*, *21*), collaborate to promote vesicle accumulation to the plasma membrane, thereby enhancing MUN priming activity at the fusion sites. In addition, Munc13 contains a RIM-binding C_2A domain that associates with the active zone scaffolding proteins (*22*–*24*), as well as a calmodulin (CaM)–binding sequence that serves as an important CaM-Ca^{2+} effector (*25*).

Neurons also require multiple specialized Ca^{2+} sensors that confer Ca^{2+} sensitivity to SNARE-mediated fusion to achieve both action potential (AP)–dependent and AP–independent types of release. AP-dependent synchronous release (<1 ms) is mainly governed by the fast Ca^{2+} sensor synaptotagmin-1 (Syt1) (*26*). The double C2 (Doc2) family proteins (*27*, *28*), another class of Ca^{2+} sensors with high Ca^{2+} affinity but slow kinetics (*29*), control AP-dependent asynchronous release (10 to 100 ms) (*30*) and AP-independent spontaneous release (*31*–*33*). Doc2A and Doc2B, the main Doc2 isoforms in the adult brain (*34*, *35*), use their double C_2 domains (C_2A and C_2B) to bind Ca^{2+} and phospholipids as well as the SNARE complex to directly induce the final fusion step (*30*, *31*), in an analogous manner to that of Syt1. However, unlike Syt1, Doc2 is largely cytosolic and contains an N-terminal Munc13-interacting domain (Mid; residues 13 to 37) preceding its C_2AB domain (*36*, *37*). Growing evidence suggests that Doc2 collaborates with Munc13 to regulate diverse activity-dependent release and plasticity in neurons (*38*–*40*), as well as different phases of secretion in neuroendocrine cells (*41*–*43*), but the underlying mechanisms remain unclear. Most previous studies ascribed the significance of the Doc2-Munc13 interaction to their strong co-accumulation to the plasma membrane in response to either phorbol 12-myristate 13-acetate (PMA) or elevated Ca^{2+} level (*37*, *44*, *45*). However, the role of this interaction on the assembly of the SNARE complex is unclear.

[1]Key Laboratory of Molecular Biophysics of the Ministry of Education, College of Life Science and Technology, Huazhong University of Science and Technology, 430074 Wuhan, China. [2]Institute for Brain Research, Wuhan Center of Brain Science, Huazhong University of Science and Technology, Wuhan 430030, China. [3]Department of Pathophysiology, School of Basic Medicine and Tongji Medical College, Huazhong University of Science and Technology, Wuhan 430030, China. [4]Department of Pathogen Biology, School of Basic Medicine, Tongji Medical College, Huazhong University of Science and Technology, 430030 Wuhan, China.
*Corresponding author. Email: cong.ma@hust.edu.cn (C.M.); lym@hust.edu.cn (Y. Lu)
†These authors contributed equally to this work.

In addition to the tight control by the presynaptic release machinery, neurotransmitter release can be constitutively and activity-dependently modulated by retrograde signaling from the postsynaptic target cells (*46*–*48*). It has become increasingly clear that synaptic adhesion molecules (SAMs) residing between the presynaptic active zones and postsynaptic density mediate multiple transsynaptic retrograde signals to alter the structure and function of presynaptic boutons (*49*–*55*). For instance, postsynaptic Neuroligin works with PSD-95 and/or N-cadherin to modulate presynaptic release by recruiting presynaptic scaffold proteins to fusion sites (*49*, *54*); postsynaptic Neuroligin or Neurexin regulates presynaptic release by influencing presynaptic metabotropic glutamate receptors or N-type calcium channel (*52*, *55*). These mechanisms involve the alteration of many aspects of presynaptic elements' properties, e.g., vesicle clustering, active zone assembly, and activity of receptors and channels. However, it remains unknown whether SAM-mediated retrograde signaling modulates neurotransmitter release by directly manipulating the release machinery. In this study, we find a potential EphB2 retrograde signaling that acutely manipulates Doc2-Munc13 interplay to control SNARE complex assembly and neurotransmitter release. We suggest that this EphB2-mediated mechanism beneficially couples the postsynaptic elements with the presynaptic release machinery to alter the structure and function of a synapse amenable for diverse neuronal activities.

RESULTS

Doc2 interacts with Munc13

Previous studies have implicated that Doc2B interacts with the Munc13-1 MUN domain via the N-terminal Mid (residues 13 to 37) (*36*, *37*). Here, we generated full-length Doc2B (FL; 1 to 412) and a series of its fragments, i.e., Doc2B (1 to 37), Doc2B (13 to 37), Doc2B (13 to 60), Doc2B (13 to 80), Doc2B (13 to 120), Doc2B (38 to 80), and Doc2B (38 to 412) (Fig. 1A), and compared their binding capacity with the Munc13-1 MUN domain (residues 933 to 1531) using glutathione *S*-transferase (GST) pull-down experiments. All the fragments, except for Doc2B (38 to 80) and Doc2B (38 to 412), showed significant binding to MUN (Fig. 1B), confirming an indispensable role of the Mid sequence (13 to 37) for Munc13-1 interaction. Intriguingly, Doc2B FL, Doc2B (13 to 60), Doc2B (13 to 80), and Doc2B (13 to 120) displayed much stronger binding capacity than Doc2B (13 to 37) (Fig. 1B), implying that additional residues downstream of the Mid sequence contribute to MUN interaction. In addition, isothermal titration calorimetry (ITC) assay showed that Doc2B FL and/or Doc2B (13 to 80) bound to MUN at a 1:1 stoichiometry, yielding a dissociation constant 10-fold higher than that of the Mid sequence (13 to 37) (Fig. 1, C and D, and table S1). Note that no detectable binding was observed for Doc2B (38 to 412) (Fig. 1D). Consistently, Doc2B (13 to 80) or Doc2B FL, rather than Doc2B (13 to 37), was capable of forming a stable heterodimeric complex with MUN, as detected by size exclusion chromatography (fig. S1A). Hence, we define residues 13 to 80 (termed Mid-L hereafter) as the intact Mid of Doc2B.

To investigate the key residues responsible for MUN interaction, we acquired ^{1}H-^{15}N heteronuclear single quantum coherence (HSQC) two-dimensional (2D) nuclear magnetic resonance (NMR) spectra of Doc2B (1 to 80) in the absence and presence of MUN, respectively. The spectrum of apo-^{15}N–labeled Doc2B (1 to 80) displayed poor dispersion of the cross peaks with ^{1}H chemical shifts ranging in 7.60 to 8.60 parts per million, indicating an unfolded conformation (Fig. 1E, black contours). Addition of unlabeled MUN caused a major reduction in the cross-peak intensities of ^{15}N-labeled Doc2B (1 to 80) (Fig. 1E, red contours), in particular for residues 13 to 50 (Fig. 1F). Among them, multiple hydrophobic residues exhibited a considerable decrease in the cross-peak intensities, suggesting their extensive participation in MUN interaction (Fig. 1E). Individual mutation I14A, I20A, I27A, I30A, I33A, and Y36A (fig. S1B) remarkably impaired binding of Doc2B FL to GST-MUN (Fig. 1G), among which I20A exhibited the strongest defect.

Next, we identified the sites in MUN responsible for Doc2B binding. MUN contains four subdomains, i.e., A, B, C, and D; we thus generated MUN-AB (859 to 1175), MUN-BC (1011 to 1407), MUN-CD (1148 to 1531), MUN-ABC (859 to 1407), and MUN-BCD (1011 to 1531) (Fig. 1A), as previously described (*12*). Detected by GST pull-down experiments, we found that Doc2B FL bound to MUN-ABC, MUN-BCD, and MUN-BC but failed to bind MUN-AB and MUN-CD (Fig. 1H), identifying subdomains B and C as the core region for Doc2B interaction. To screen the binding sites, we designed a series of mutations on the surface of MUN-BC and measured their binding with Doc2B FL (fig. S1C). Among them, N1128A/F1131A (NFAA) and W1165A significantly impaired Doc2B interaction (Fig. 1I). Last, we verified the importance of I20 in Doc2B and N1128/F1131 (NF) in Munc13-1 for Doc2B–Munc13-1 interaction in human embryonic kidney (HEK) 293 cells. In line with previous results (*37*, *40*), we observed cotranslocation of mCherry-tagged Doc2B wild-type (WT) with enhanced green fluorescent protein (EGFP)–tagged Munc13-1 (C_1C_2BMUN) to the plasma membrane upon PMA stimulation (fig. S1D). However, either I20A or NFAA mutation strongly impaired their cotranslocation (fig. S1D). Together, these data reveal that the Mid-L in Doc2B and the NF sequence in Munc13-1 mediate Doc2B–Munc13-1 interaction.

Doc2-Munc13 interaction inhibits SNARE complex assembly

Previous results have shown that the NF (N1128/F1131) pocket of Munc13-1 mediates opening of Syx1, thus promoting the transition from the Munc18-1/Syx1 complex to the SNARE complex (*12*, *13*). Our finding that Doc2B binds the Munc13-1 NF pocket via Mid-L leads to a hypothesis that Doc2B would hinder Munc13-1 from catalyzing SNARE complex assembly. To test this hypothesis, we monitored MUN-catalyzed SNARE complex assembly starting from the Munc18-1/Syx1 complex in the presence of Syb2 and SN25 by fluorescence resonance energy transfer (FRET) assay as previously described (Fig. 2A) (*12*). Intriguingly, MUN-catalyzed SNARE complex assembly was partially inhibited by Doc2B Mid and totally abrogated by Doc2B Mid-L or Doc2B FL (Fig. 2B). Notably, this inhibition by Doc2B Mid displayed a dose-dependent effect (Fig. 2C), reflecting the predominant role of the Mid sequence in the inhibition. Then, we investigated whether disruption of Doc2B-MUN interaction can initiate MUN-catalyzed SNARE complex assembly. The MUN NFAA mutation that disrupts Doc2B interaction failed to initiate the assembly (Fig. 2D); this is expected because this mutation intrinsically blocks MUN catalytic activity (*12*). Intriguingly, the Doc2B I20A mutation that impairs MUN interaction almost fully recovered MUN-catalyzed SNARE complex assembly (Fig. 2D). These observations were further validated by previously established native-polyacrylamide gel electrophoresis (PAGE) experiments (fig. S2) (*56*). Thus, these results demonstrate that Doc2B–Munc13-1 interaction inhibits Munc13-catalyzed SNARE complex assembly.

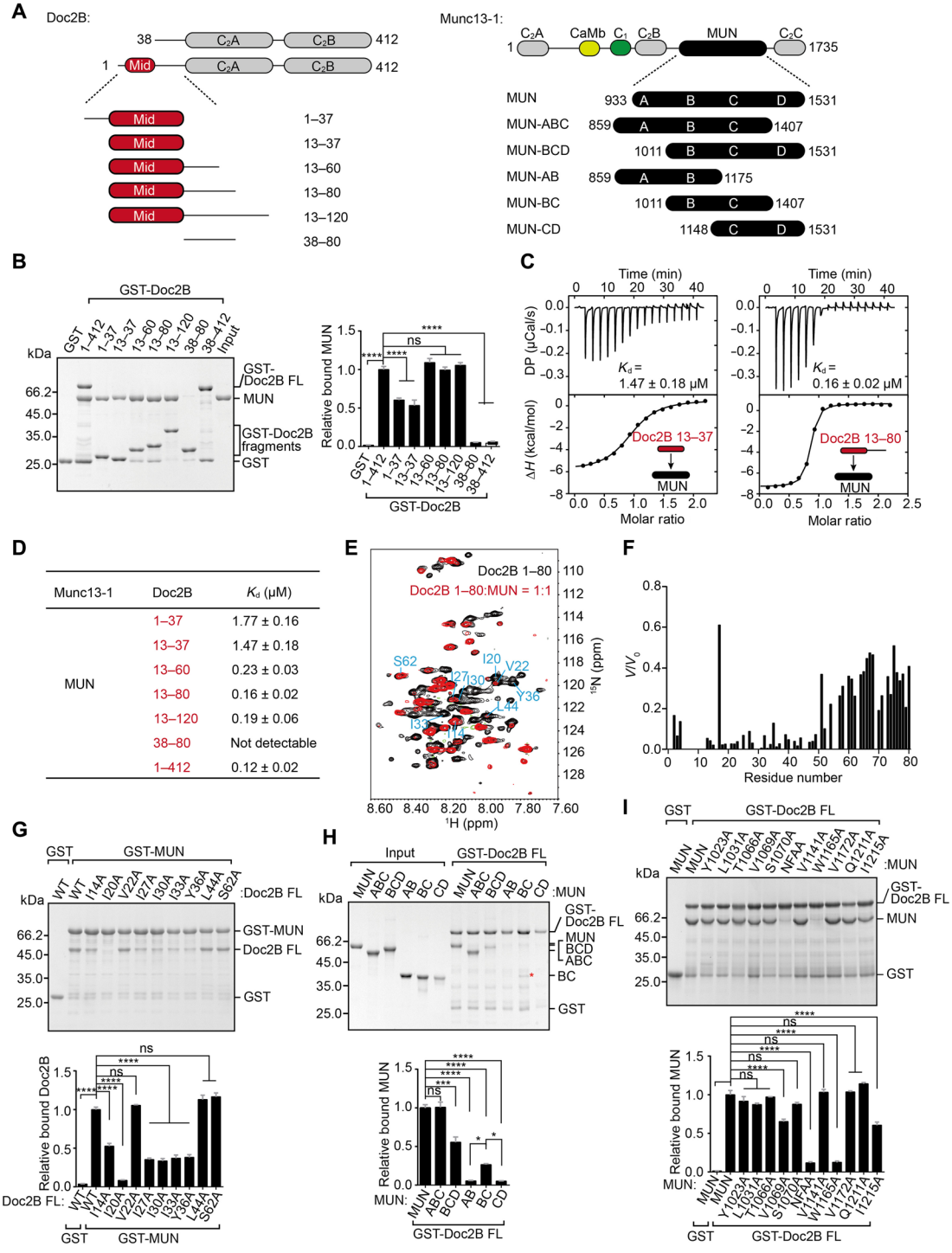

Munc13-1	Doc2B	K_d (μM)
MUN	1–37	1.77 ± 0.16
	13–37	1.47 ± 0.18
	13–60	0.23 ± 0.03
	13–80	0.16 ± 0.02
	13–120	0.19 ± 0.06
	38–80	Not detectable
	1–412	0.12 ± 0.02

Fig. 1. Doc2B interacts with Munc13-1. (**A**) Schematic diagram showing domain organization and variant fragments of Doc2B and Munc13-1. (**B**) Binding of MUN to GST-Doc2B FL or its variant fragments measured by GST pull-down experiments and quantification of the binding. (**C**) ITC-based measurements of MUN binding to GST-Doc2B 13 to 37 (Mid, left) and to GST-Doc2B 13 to 80 (Mid-L, right). (**D**) ITC-based measurements of the binding affinities between GST-Doc2B FL or its variant fragments and MUN. (**E**) 2D ^{1}H-^{15}N HSQC spectra of ^{13}C/^{15}N-labeled Doc2B 1 to 80 before (black) and after (red) addition of MUN. Cross-peaks of residues that are chosen for mutation to detect MUN binding are labeled along with their corresponding residue number (cyan). (**F**) Peak intensity alteration of ^{13}C/^{15}N-labeled Doc2B 1 to 80 protein expressed as ratio between integrated peak volumes after (V) and before (V_0) addition of unlabeled MUN. (**G**) Binding of Doc2B FL or its variant mutations to GST-MUN measured by GST pull-down experiments and quantification of the binding. (**H**) Binding of MUN or its variant fragments to GST-Doc2B FL measured by GST pull-down experiments and quantification of the binding. Red asterisk shows the band of bound MUN-BC. (**I**) Binding of MUN or its variant mutations to GST-Doc2B FL measured by GST pull-down experiments and quantification of the binding. Data of GST pull-down experiments are processed by ImageJ (National Institutes of Health) and presented as means ± SEM (n = 3). Statistical significance and P values were determined by one-way analysis of variance (ANOVA) with Tukey's multiple comparisons test. *P < 0.05; ***P < 0.001; ****P < 0.0001; ns, not significant.

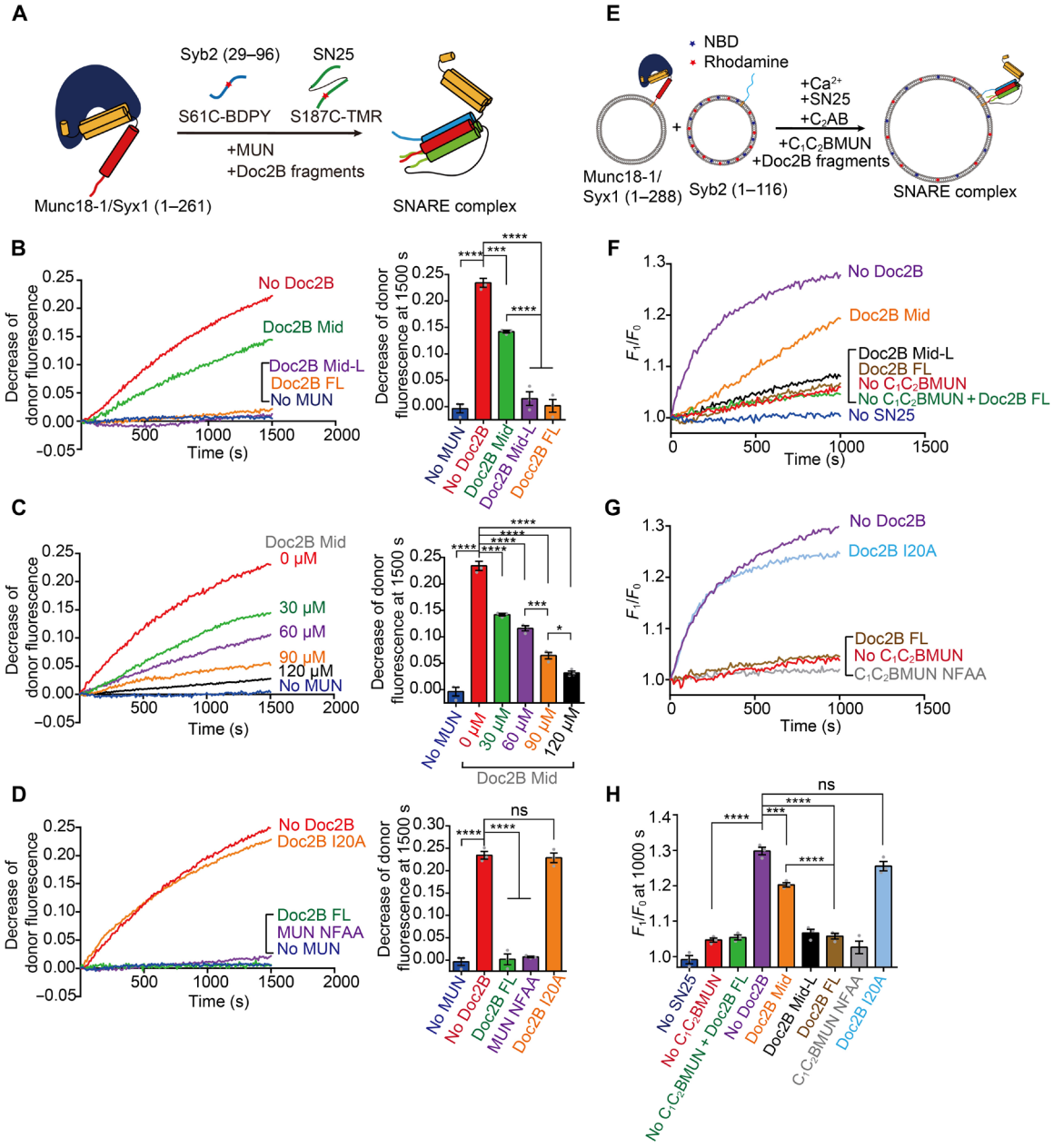

Fig. 2. Doc2B inhibits MUN-catalyzed SNARE complex assembly and membrane fusion. (**A**) Illustration of the FRET assay for detecting MUN-catalyzed SNARE complex assembly starting from the Munc18-1/Syx1 (1 to 261) complex in the presence of Syb2 (29 to 96), SN25, and MUN. FRET signal between BDPY-labeled Syb2 S61C (donor) and TMR-labeled SN25 S187C (acceptor) was monitored. (**B** to **D**) MUN-catalyzed SNARE complex assembly by addition of Doc2B Mid, Doc2B Mid-L, or Doc2B FL, respectively (B), addition of different concentrations of Doc2B Mid (C), and addition of MUN NFAA or Doc2B I20A, which disrupts Doc2B-MUN interaction (D). Decrease of donor fluorescence at 1500 s is shown in the column at the right of the chart. (**E**) Illustration of Munc13-catalyzed lipid mixing between liposomes bearing Syb2 (1 to 116) and liposomes bearing the Munc18-1/Syx1 (1 to 288) complex in the presence of SN25, Syt1 C2AB, Ca^{2+}, and Munc13-1 (C_1C_2BMUN). Donor (NBD) fluorescence was monitored at 538 nm. (**F** to **H**) Munc13-catalyzed lipid mixing by addition of Doc2B Mid, Doc2B Mid-L, or Doc2B FL, respectively (F); addition of C_1C_2BMUN NFAA or Doc2B I20A (G). Munc13-catalyzed lipid mixing at 1000 s is shown in (H). F_1, fluorescence intensity observed as a function time; F_0, initial fluorescence intensity. Data are presented as means ± SEM ($n = 3$). Statistical significance and P values were determined by one-way ANOVA with Tukey's multiple comparisons test. *$P < 0.05$; ***$P < 0.001$; ****$P < 0.0001$.

To explore the effect of Doc2B-MUN interaction on SNARE-dependent membrane fusion, we performed lipid-mixing experiments using liposomes containing the Munc18-1/Syx1 (full-length) complex and liposomes bearing Syb2 (full-length) in the presence of Munc13-1 (C_1C_2BMUN), SN25, Syt1-C_2AB, and Ca^{2+} (Fig. 2E). Consistent with the assembly results, Doc2B Mid partially impaired, but Doc2B Mid-L and Doc2B FL strongly impaired, Munc13-1 activity in catalyzing SNARE-mediated membrane fusion (Fig. 2, F and H). Disruption of Doc2B-MUN interaction by introducing the I20A mutation completely rescued Munc13-1 activity (Fig. 2, G and H). Hence, these results demonstrate that Doc2B–Munc13-1 interaction inhibits Munc13 activity in catalyzing SNARE-mediated membrane fusion.

EphB2 associates with the release machinery and directly binds Doc2

How could Munc13-1 escape Doc2B inhibition to execute its essential function in SNARE complex assembly? Phosphorylation is an effective way to modulate protein structure and protein-protein interaction. We hence detected whether Doc2B undergoes phosphorylation. We targeted Src, Fyn, epidermal growth factor receptor (EGFR), EphB2, TrkA, TrkB, Fak2, and Tec2 as potential tyrosine kinase (*57*, *58*) and performed in vitro phosphorylation assays using GST-tagged Doc2B Mid. Among the candidates, we found that EphB2 specifically phosphorylated Doc2B (fig. S3A).

EphB2, a SAM that has tyrosine kinase activity, is widely distributed at pre- and postsynaptic membranes (*59*–*61*) and is critical for synaptic development, formation, and plasticity (*62*–*64*). Analysis of the expression pattern of Doc2B and EphB2 in adult mouse brain indicated their codistribution in the hippocampus, particularly in the CA1 region and the dentate gyrus (Fig. 3A). Immunofluorescence analysis of primary cultured mouse hippocampal neurons showed the presence of EphB2 in puncta within the dendrites (fig. S3B). These puncta were found to colocalize with Doc2B and the endogenous presynaptic vesicle marker VAMP2 (fig. S3B). Then, we purified synaptosomes and separated pre- and postsynaptic elements, respectively, and found that EphB2 was localized in both pre- and postsynaptic compartments (Fig. 3B). Doc2B was predominantly associated with presynaptic element Munc13-1 and Munc18-1 but excluded from postsynaptic marker PSD-95 (Fig. 3B). Therefore, Doc2B probably serves as a downstream effector of presynaptic EphB2.

We next explore the interaction between Doc2B and EphB2. Through GST pull-down experiments combined with immunoblotting, we observed binding of EphB2, along with crucial presynaptic components such as Munc13-1, RIM-1, Munc18-1, Syx1, and SN25, to GST-Doc2B FL in mouse brain homogenate lysates (fig. S3C). Notably, the strength of binding varied among these components, indicating different levels of association between EphB2 and the release machinery in presynaptic active zones. Then, we verified the interaction between Doc2B and EphB2 in HEK293 cells. mCherry-tagged Doc2B coimmunoprecipitated with Flag-tagged EphB2 and vice versa (Fig. 3, C and D). Next, we aim to identify the specific region of EphB2 responsible for Doc2B interaction in HEK293 cells (Fig. 3E). Intriguingly, Doc2B bound notably to EphB2-ΔSP, which lacks the C-terminal sterile α motif and the PDZ-binding module (Fig. 3F). However, Doc2B failed to bind EphB2-ΔKSP, which additionally lacks the kinase domain (Fig. 3F), suggesting the requirement of the kinase domain for Doc2B interaction. Moreover, the EphB2 K653R (KR) mutation that terminates EphB2 kinase activity failed to bind Doc2B (Fig. 3G). These data indicate that an active form of the EphB2 kinase domain is indispensable for Doc2B interaction.

EphB2 phosphorylates Doc2

Doc2B Mid-L contains only one tyrosine residue (Y36), which is highly conserved across Doc2 family proteins (fig. S3D) and plays a critical role in MUN interaction (Fig. 1G). We hence generated a phosphorylation state-specific antibody (termed pY36) and investigated whether EphB2 phosphorylates Doc2B at Y36 using in vitro phosphorylation assay. The pY36 antibody was generated by the modified peptide (QISDY-pFPRF, residues 32 to 40 of Doc2B) and demonstrated by dot blot analysis (fig. S3E). GST-Doc2B Mid, Mid-L, and FL were substantially phosphorylated by the kinase domain (residues 595 to 906) of EphB2, detected by immunoblotting with pY36 or pTyr antibody (Fig. 3H). However, introduction of the unphosphorylatable mutation Y36F in Doc2B or the treatment of phosphatase (APase) diminished EphB2-dependent Doc2B phosphorylation (Fig. 3I). In contrast, GST alone, the Munc13-1 MUN domain, Munc18-1, Syx1, and SN25 cannot be phosphorylated by the kinase domain of EphB2 (fig. S3F).

Then, we explored the phosphorylation of Doc2B by EphB2 in HEK293 cells. In contrast to Doc2B WT, mCherry-tagged Doc2B Y36F showed greatly reduced EphB2-dependent phosphorylation (Fig. 3J). Similarly, Flag-tagged EphB2 KR, which loses kinase activity, failed to phosphorylate Doc2B (Fig. 3K). In addition, the EphB2 Y596E/Y602E mutant (YYEE), which retains kinase activity but cannot activate downstream Src family proteins, still phosphorylated Doc2B (Fig. 3K). This suggests that EphB2 directly phosphorylates Doc2B independent of the downstream Src pathway. In contrast, EphA4, another Eph family protein present in presynaptic membranes (*61*), was unable to phosphorylate Doc2B (fig. S3G). Together, these data suggest that EphB2 directly and specifically phosphorylates Doc2B at residue Y36.

Under physiological conditions, the kinase activity of EphB2 can be potentiated by postsynaptic EphrinB-1, EphrinB-2, or EphrinB-3 (*65*). In our study, we observed that EGFP-tagged EphB2 located on the plasma membrane and exhibited a higher binding affinity for exogenously applied EphrinB2 or EphrinB3 compared to EphrinB1 in HEK293 cells (fig. S3H). Next, we focused on EphrinB3 and tested whether it could activate EphB2 and trigger Doc2B phosphorylation in cultured mouse cortex neurons. Immunoblotting results showed that the addition of EphrinB3 in cultured neurons led to substantial phosphorylation of EphB2 (Fig. 3L), indicating the activation of EphB2 by EphrinB3. Furthermore, stimulation of cultured neurons with EphrinB3 resulted in an increase in the level of Doc2B phosphorylation (Fig. 3L). In line with this observation, immunofluorescence analysis showed that addition of EphrinB3 to cultured neurons significantly increased the puncta number of phosphorylated Doc2B (fig. S3I). These results suggest that the elevated EphrinB3-EphB2 signaling enhances Doc2B phosphorylation. To further investigate the phosphorylation of Doc2B by EphB2, we analyzed EphB2 WT ($EphB2^{+/+}$) and deficient ($EphB2^{-/-}$) mouse brains. Immunoblotting analysis using the pY36 antibody demonstrated that the deletion of EphB2 resulted in a notable decrease in the level of Doc2B phosphorylation (Fig. 3M). Last, we suppressed endogenous Doc2B expression in Doc2A-deficient mice and found that the acute knockdown of Doc2B led to significant decrease in the level of Doc2B expression and Doc2B phosphorylation in the lysates of mouse brain homogenates (Fig. 3N). These findings suggest a potential retrograde signaling pathway from postsynaptic EphrinB3 to presynaptic EphB2, which regulates the phosphorylation of Doc2B at Y36.

EphB2-dependent Doc2 phosphorylation attenuates Doc2-Munc13 interaction to recover SNARE complex assembly

We explored whether EphB2-dependent Doc2B Y36 phosphorylation affects its interaction with MUN. We observed that the unphosphorylatable mutant, Doc2B Y36F, bound to GST-MUN as effectively as Doc2B WT. Conversely, the phosphomimetic mutant, Doc2B Y36D, displayed significantly reduced binding to GST-MUN (Fig. 4A). These findings were further supported by Doc2B's binding to full-length Munc13-1 from mouse brain tissues (fig. S4A). In addition, we measured the binding affinity of Doc2B mutants with MUN using

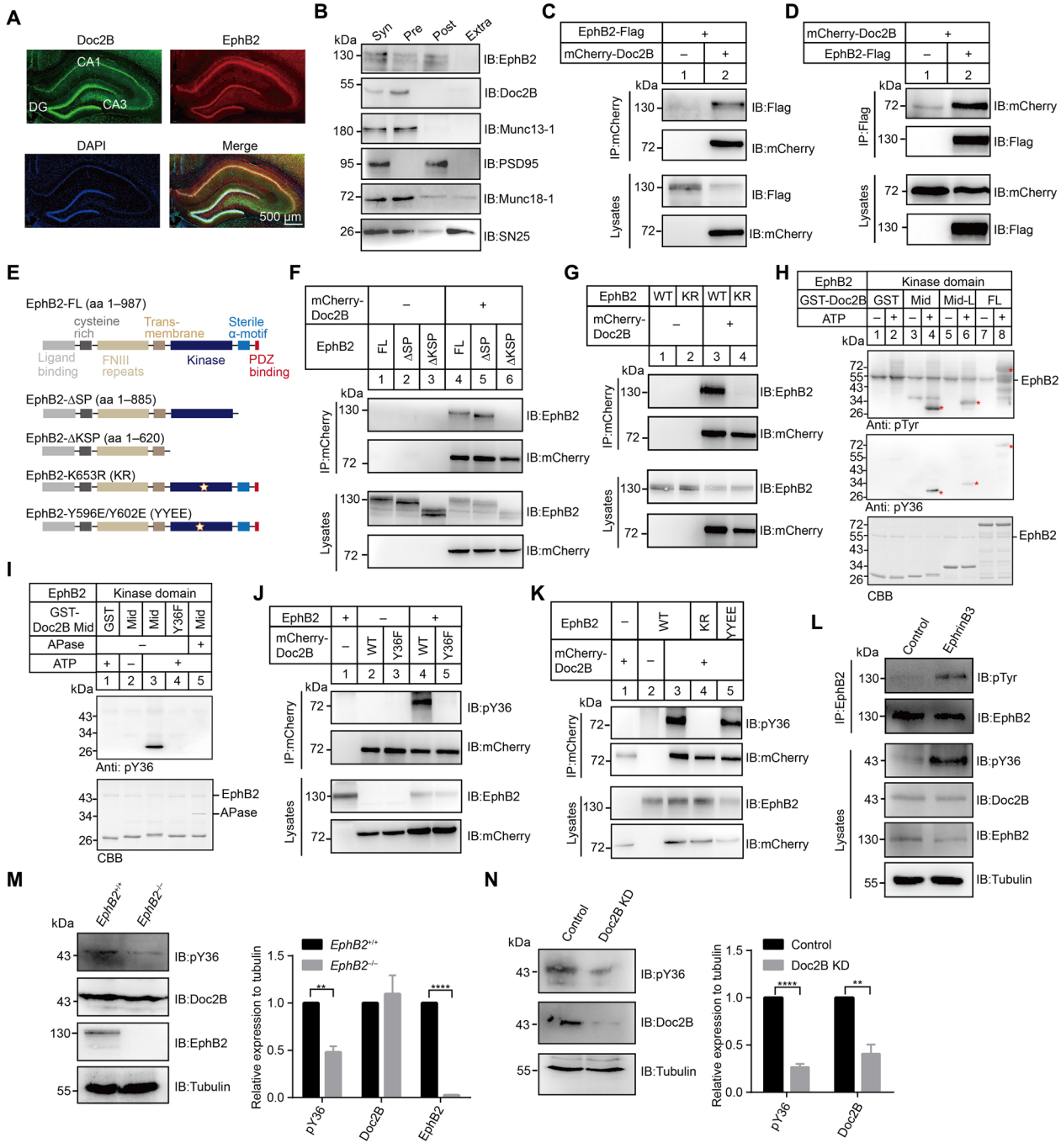

Fig. 3. Presynaptic EphB2 interacts with Doc2B and phosphorylates Doc2B at Y36. (**A**) Immunostaining against Doc2B (green) and EphB2 (red) in the mouse hippocampus region. Nuclear DNA was labeled with 4′,6-diamidino-2-phenylindole (DAPI) (blue). Scale bars, 500 μm. (**B**) Separation of pre- and postsynaptic densities from purified synaptosomes. Syn, synaptosome; Pre, presynaptic elements; Post, postsynaptic elements; Extra, extrajunctional synaptic elements. (**C** and **D**) Western blot analysis of Doc2B-EphB2 interaction following cotransfection of mCherry-tagged Doc2B and Flag-tagged EphB2 in HEK293 cells. Cell lysates were immunoprecipitated by anti-mCherry antibody (C) or anti-Flag antibody (D), followed by immunoblotting with indicated antibody. (**E**) Schematic representation of EphB2 constructs. (**F** and **G**) Western blot analysis of Doc2B-EphB2 interaction following cotransfection of various combinations of plasmids containing EphB2 FL, EphB2-ΔSP, EphB2-ΔKSP, and/or mCherry-tagged Doc2B (F), EphB2 WT, KR, and/or mCherry-tagged Doc2B (G) in HEK293 cells. (**H** and **I**) In vitro phosphorylation assay using sumo-tagged EphB2 and GST-tagged Doc2B fragments (H) and GST-tagged Doc2B Mid or Y36F (I) in the presence or absence of ATP and APase. Asterisks show bands of GST-Doc2B Mid, Mid-L, and FL, respectively. CBB, Coomassie Brilliant Blue staining. (**J** and **K**) Western blot analysis of Doc2B phosphorylation following cotransfection of mCherry-tagged Doc2B WT or Y36F and/or EphB2 (J) and EphB2 WT, KR, or YYEE and/or mCherry-tagged Doc2B (K) in HEK293 cells. (**L**) Detection of Doc2B phosphorylation in cultured mouse cortex neurons by application of Fc (control) or preclustered Ephrin-B3-Fc. (**M** and **N**) Western blot analysis of Doc2B phosphorylation in *EphB2*$^{+/+}$ or *EphB2*$^{-/-}$ mouse brains (M) in Doc2A-deficient neurons infected with Doc2B KD or control virus (N). Tubulin used as the reference protein. Data are presented as means ± SEM ($n = 3$). Statistical significance and *P* values were determined by Student's *t* test (**$P < 0.01$; ****$P < 0.0001$).

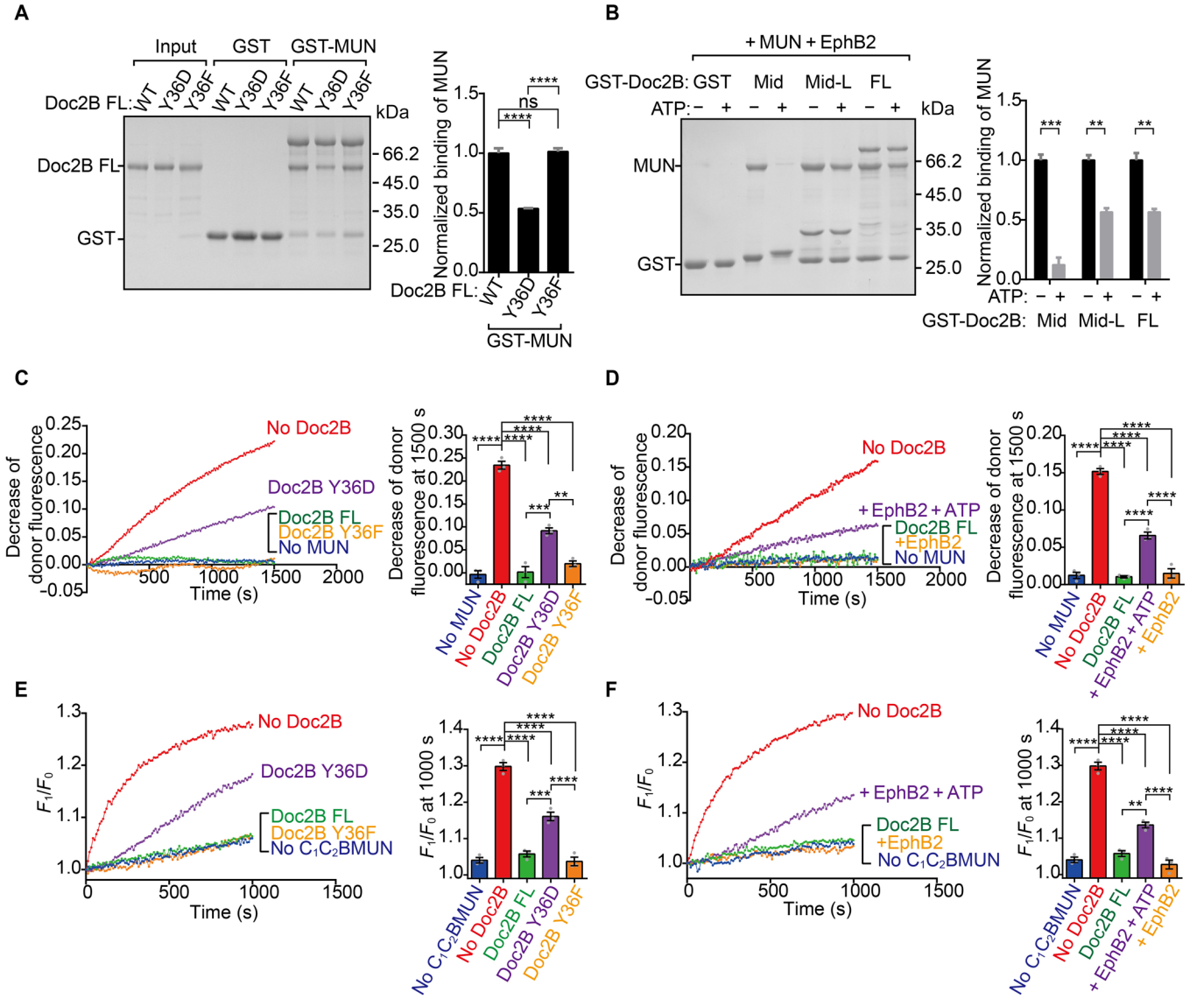

Fig. 4. Doc2B phosphorylation by EphB2 relieves inhibition of Doc2B on Munc13-catalyzed SNARE complex assembly and membrane fusion. (**A**) Binding of Doc2B WT or its phosphomimetic/unphosphorylatable mutations to GST-MUN measured by GST pull-down experiments and quantification of the binding. (**B**) Binding of the MUN domain to GST-Doc2B fragments and EphB2 mixture measured by GST pull-down experiments in the presence or absence of ATP and quantification of the binding. (**C** and **D**) MUN-catalyzed SNARE complex assembly by addition of Doc2B WT, Y36D, or Y36F, respectively (C), and addition of Doc2B WT and EphB2 mixture in the presence or absence of ATP (D). Decrease of donor fluorescence at 1500 s is shown in the column at the right of the chart. (**E** and **F**) Munc13-catalyzed lipid mixing by addition of Doc2B WT, Y36D, or Y36F, respectively (E), and addition of Doc2B WT and EphB2 mixture in the presence or absence of ATP (F). Munc13-catalyzed lipid mixing at 1000 s is shown in the column at the right of the chart. F_1, fluorescence intensity observed as a function time; F_0, initial fluorescence intensity. Data are presented as means ± SEM ($n = 3$). Statistical significance and P values were determined by one-way ANOVA with Tukey's multiple comparisons test. $^{**}P < 0.01$; $^{***}P < 0.001$; $^{****}P < 0.0001$.

ITC assay (table S1). Doc2B Y36F exhibited nearly identical thermodynamic properties when binding to MUN compared to Doc2B FL. However, Doc2B Y36D bound to MUN with a notably reduced affinity. Furthermore, similar to Doc2B Y36D, the addition of EphB2 significantly impaired Doc2B binding to MUN in the presence of adenosine triphosphate (ATP) (Fig. 4B). Hence, the above data suggest that EphB2-dependent Doc2B Y36 phosphorylation attenuates Doc2B-MUN interaction.

We then explored whether EphB2-dependent Doc2B Y36 phosphorylation would alleviate Doc2B inhibitory effect on Munc13-1 activity in SNARE complex assembly and membrane fusion. To this aim, we carried out FRET assay and found that Doc2B Y36D, which impairs MUN interaction, significantly recovered Munc13-catalyzed SNARE complex assembly and membrane fusion (Fig. 4, C and E). However, Doc2B WT and Doc2B Y36F, which retain MUN interaction, inhibited Munc13-catalyzed SNARE complex assembly and membrane fusion (Fig. 4, C and E). EphB2 treatment on Doc2B WT clearly restored Munc13-catalyzed SNARE complex assembly and membrane fusion in the presence of ATP (Fig. 4, D and F). Hence, EphB2-dependent Doc2B Y36 phosphorylation attenuates

Doc2B-MUN interaction, therefore activating Munc13-catalyzed SNARE complex assembly and membrane fusion. These results suggest that EphB2 functions as a molecular switch, facilitating the transition of the Doc2B–Munc13-1 complex from an associated state to a dissociated state.

Modulation of Doc2-Munc13 interaction by EphB2 controls spontaneous release and synaptic augmentation

We next investigate whether other members of Doc2 family proteins operate similarly to Doc2B. Doc2 family proteins contain Doc2A, Doc2B, and Doc2C (*34*, *66*). Similar to Doc2B, Doc2A and Doc2C bound to MUN via Mid-L (fig. S5A). EphB2 likewise enabled Doc2A phosphorylation at Y35, which attenuates Doc2A-MUN interaction, thereby promoting SNARE complex assembly (fig. S5, B to E). These results indicate a common function shared by Doc2A and Doc2B. Considering the predominant expression of Doc2A in neurons compared to the ubiquitous expression of Doc2B (*34*, *67*), we consequently generated a mutant mouse line with a complete deletion of Doc2A ($Doc2A^{-/-}$ mice; fig. S6A), as previously reported (*68*). In $Doc2A^{-/-}$ mice, several proteins crucial for synaptic transmission, such as Munc13-1, Munc18-1, EphB2, Syt1, and SNAREs, were expressed at normal levels compared to that in $Doc2A^{+/+}$ mice (fig. S6, B and C). In addition, $Doc2A^{-/-}$ mice were viable and exhibited no discernible differences in size or gross behavior compared to their WT littermates. To investigate the impact of Doc2A deletion in neurotransmitter release, we performed whole-cell patch clamp recordings in cultured mouse cortex neurons from $Doc2A^{-/-}$ mice. We found that the mean amplitude of evoked excitatory postsynaptic currents (EPSCs) was unchanged in $Doc2A^{-/-}$ neurons compared to $Doc2A^{+/+}$ neurons (fig. S6, D and E). However, the deletion of Doc2A significantly reduced the frequency of miniature EPSCs (mEPSCs; fig. S6, F to H), which is consistent with the essential role of Doc2 in spontaneous release (*31*).

Since our in vitro experiments were primarily focused on Doc2B and that the pan-neuronal expression of the Doc2B protein was reported to successfully rescue spontaneous release or synaptic augmentation in neurons lacking Doc2A and/or Doc2B (*31*, *33*, *40*), we chose to express Doc2B in Doc2A-deficient neurons and explore the effect of the association and dissociation of Doc2B–Munc13-1 on neurotransmitter release. Expression of either Doc2A or Doc2B was able to rescue spontaneous release in $Doc2A^{-/-}$ neurons (Fig. 5, A and B). Consistent with previous studies (*33*), a mutant version of Doc2B, D303N, which disrupts its C_2B Ca^{2+}-binding site, was unable to rescue spontaneous release (Fig. 5, C and D), indicating that Doc2B sensing Ca^{2+} is important for spontaneous release. Intriguingly, Doc2B (81 to 412, lacking Mid-L) or Doc2B I20A, which impairs Munc13-1 interaction, also failed to rescue spontaneous release (Fig. 5, C and D), suggesting that the association of Doc2B and Munc13-1 is important for spontaneous release.

We next tested whether the dissociation of Doc2B with Munc13-1, which is mediated by Doc2B phosphorylation, is required for spontaneous release. Consistent with our in vitro results (Fig. 4), expression of Doc2B Y36F, which constantly binds Munc13-1, was unable to rescue spontaneous release in $Doc2A^{-/-}$ neurons (Fig. 5, C and D). Similarly, expression of Doc2B Y36D, which mimics a constantly phosphorylated state, still failed to rescue spontaneous release (Fig. 5, C and D). This result is expected, as the Y36D mutation disrupts the interaction between Doc2B and Munc13-1, which renders Doc2B unable to target to Munc13-1–enriched fusion sites (fig. S1D). To test whether the above Doc2B mutants could properly localize to synapse, we generated N-terminal Flag-tagged fusion proteins of the above Doc2B mutants. Immunofluorescence analysis showed a substantial enrichment of Flag-tagged Doc2B mutants within most VAMP2 puncta in $Doc2A^{-/-}$ neurons (fig. S7A), indicating the proper localization of the Doc2B mutants. Furthermore, there was no notable change in the number of synapses rescued by the Doc2B mutants in $Doc2A^{-/-}$ neurons (fig. S7B). Together, these results suggest that the association and dissociation of Doc2B–Munc13-1 is important for spontaneous release.

Since EphB2 is able to facilitate the transition of Doc2B–Munc13-1 complex from an associated state to a dissociated state in vitro, we aimed to verify this function in spontaneous release. We used exogenously supplied EphrinB3 to activate EphB2 and found that it led to a gradual increase in the frequency of mEPSC in $Doc2A^{+/+}$ neurons but not in $Doc2A^{-/-}$ neurons in a time course of 70 min (Fig. 5, E and F). The increment of spontaneous release was only restored upon the expression of Doc2B WT but not Doc2B Y36F in $Doc2A^{-/-}$ neurons (Fig. 5G). These data suggest that EphrinB3-EphB2 signaling increases spontaneous release by facilitating the association-dissociation transition of Doc2B–Munc13-1.

Besides, Doc2 was recently implicated to regulate synaptic augmentation together with Munc13 (*40*). We next explored whether the association and dissociation of Doc2B–Munc13-1 is required for augmentation. To induce augmentation, we stimulated cultured mouse cortex neurons at 10 Hz for 5 s and observed a robust increase in the amplitude of EPSC in response to single APs (Fig. 5, H and I); this enhancement lasts for tens of seconds in $Doc2A^{+/+}$ neurons. This augmentation was eliminated in $Doc2A^{-/-}$ neurons but could be rescued by expressing exogenous Doc2B WT (Fig. 5J). Notably, the rescue effect was not observed with Doc2B Y36D or I20A (Fig. 5J), indicating the requirement of the association of Doc2B–Munc13-1 for augmentation. In addition, Doc2B Y36F, which retains Munc13-1 interaction but assumes in an unphosphorylatable state, only slightly rescued augmentation (Fig. 5J), suggesting that the dissociation of Doc2B–Munc13-1, mediated by Doc2B phosphorylation, is also important for augmentation. These data suggest that the association and dissociation of Doc2B–Munc13-1 contributes to activity-dependent plasticity.

Disruption of Doc2 interplay with Munc13 impairs spatial learning and memory

Next, we asked whether the direct and functional interplay between Doc2 and Munc13 is associated with brain function, such as spatial learning and memory. We first expressed Doc2B Mid-L or its mutants in cultured mouse cortex neurons to interfere Munc13 function and examined its effect on synaptic transmission. Introduction of Mid-L or Mid-L Y36F that impairs the Doc2-Munc13 interplay significantly inhibited the mEPSC frequency and AP-evoked EPSC amplitude (Fig. 6, A to D). In contrast, Mid-L I20A or Mid-L Y36D with weak influence on the Doc2-Munc13 interplay had no effect on both mEPSC and evoked EPSC (Fig. 6, A to D). Upon characterizing the size of the readily releasable pool (RRP), we observed that Mid-L and Mid-L Y36F, but not Mid-L I20A and Mid-L Y36D, led to a great reduction in RRP size (Fig. 6, E and F). This indicates that the disruption of the interaction between Doc2 and Munc13 results in defective priming of exocytosis. To confirm the subcellular localization of the Flag-tagged Doc2B Mid-L mutants, we performed immunofluorescence staining and found that all of the mutants were dispersed in the soma and dendrites, partially colocalizing with the endogenous presynaptic marker

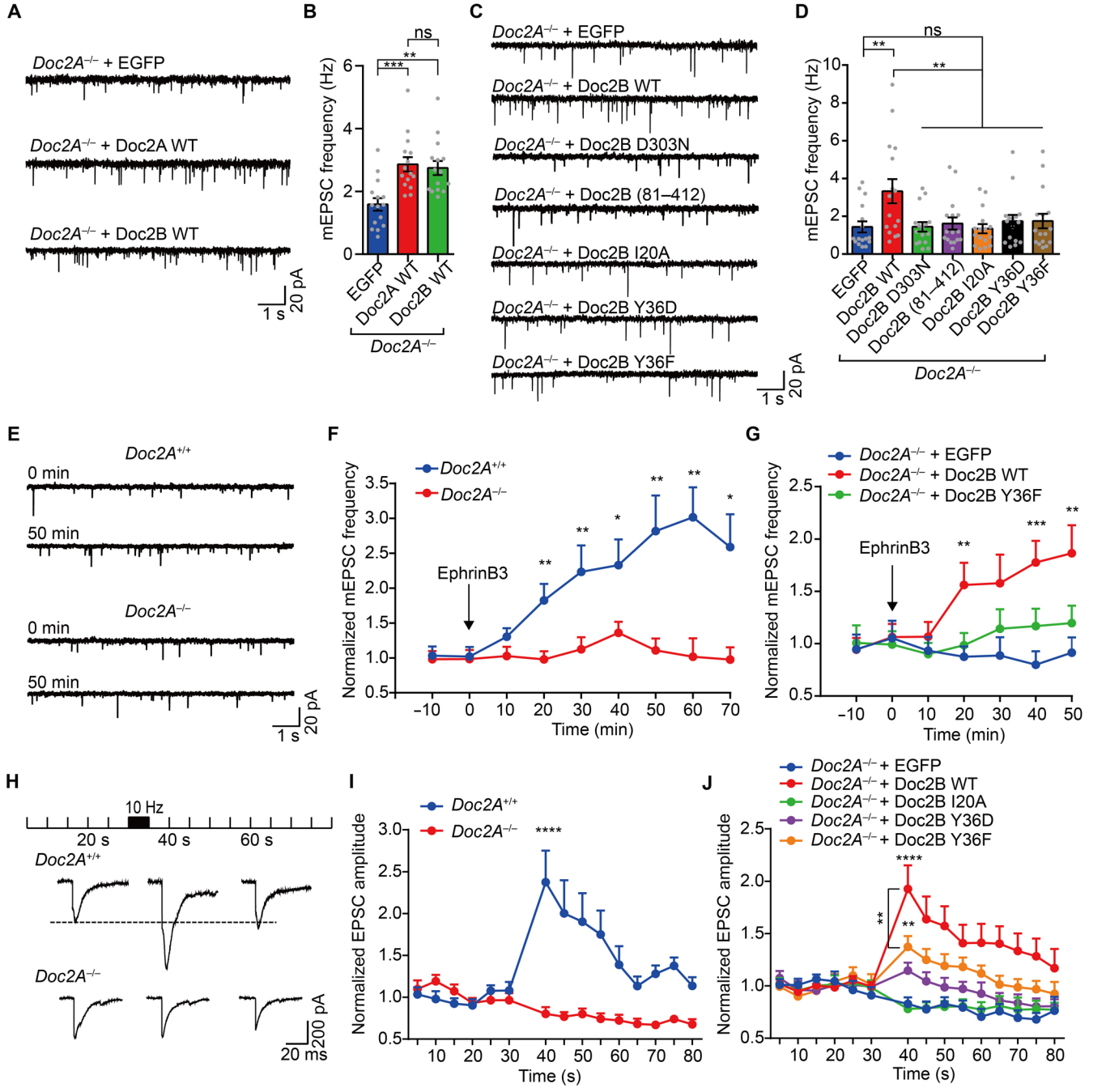

Fig. 5. EphrinB3-EphB2 signaling regulates spontaneous release and synaptic augmentation. (**A** and **B**) Representative traces (A) and quantification of mEPSC frequency (B) in *Doc2A*$^{-/-}$ neurons (EGFP, $n = 15$; Doc2A WT, $n = 15$; Doc2B WT, $n = 15$). (**C** and **D**) Representative traces (C) and quantification of mEPSC frequency (D) in *Doc2A*$^{-/-}$ neurons expressing EGFP ($n = 16$), Doc2B WT ($n = 16$), Doc2B D303N ($n = 16$), Doc2B (81 to 412) ($n = 16$), or Doc2B I20A ($n = 16$). (**E**) Representative traces of mEPSC frequency in *Doc2A*$^{+/+}$ (top) and *Doc2A*$^{-/-}$ (bottom) neurons after stimulation with EphrinB3. (**F** and **G**) Summary of the changes in mEPSC frequency after stimulation with EphrinB3 in *Doc2A*$^{+/+}$ ($n = 16$) and *Doc2A*$^{-/-}$ ($n = 18$) neurons (F) and in *Doc2A*$^{-/-}$ neurons expressing EGFP ($n = 16$), Doc2B WT ($n = 16$), or Doc2B Y36F ($n = 16$) (G). Data were normalized to the average value during the control period before stimulation. (**H**) Representative traces of evoked EPSCs in synaptic augmentation at 20, 40, and 60 s in *Doc2A*$^{+/+}$ and *Doc2A*$^{-/-}$ neurons. (**I** and **J**) Normalized peak amplitudes of evoked EPSCs in *Doc2A*$^{+/+}$ ($n = 20$) and *Doc2A*$^{-/-}$ ($n = 23$) neurons (I) or in *Doc2A*$^{-/-}$ neurons expressing EGFP ($n = 16$), Doc2B WT ($n = 16$), Doc2B I20A ($n = 17$), Doc2B Y36D ($n = 15$), or Doc2B Y36F ($n = 15$) (J). Data are presented as means ± SEM. Recorded cells are from three independent experiments. Statistical significance and *P* values for (B), (D), (G), and (J) were determined by one-way ANOVA with Dunnett's multiple comparison test, and those for (F) and (I) were determined by Student's *t* test. *$P < 0.05$; **$P < 0.01$; ***$P < 0.001$; ****$P < 0.0001$.

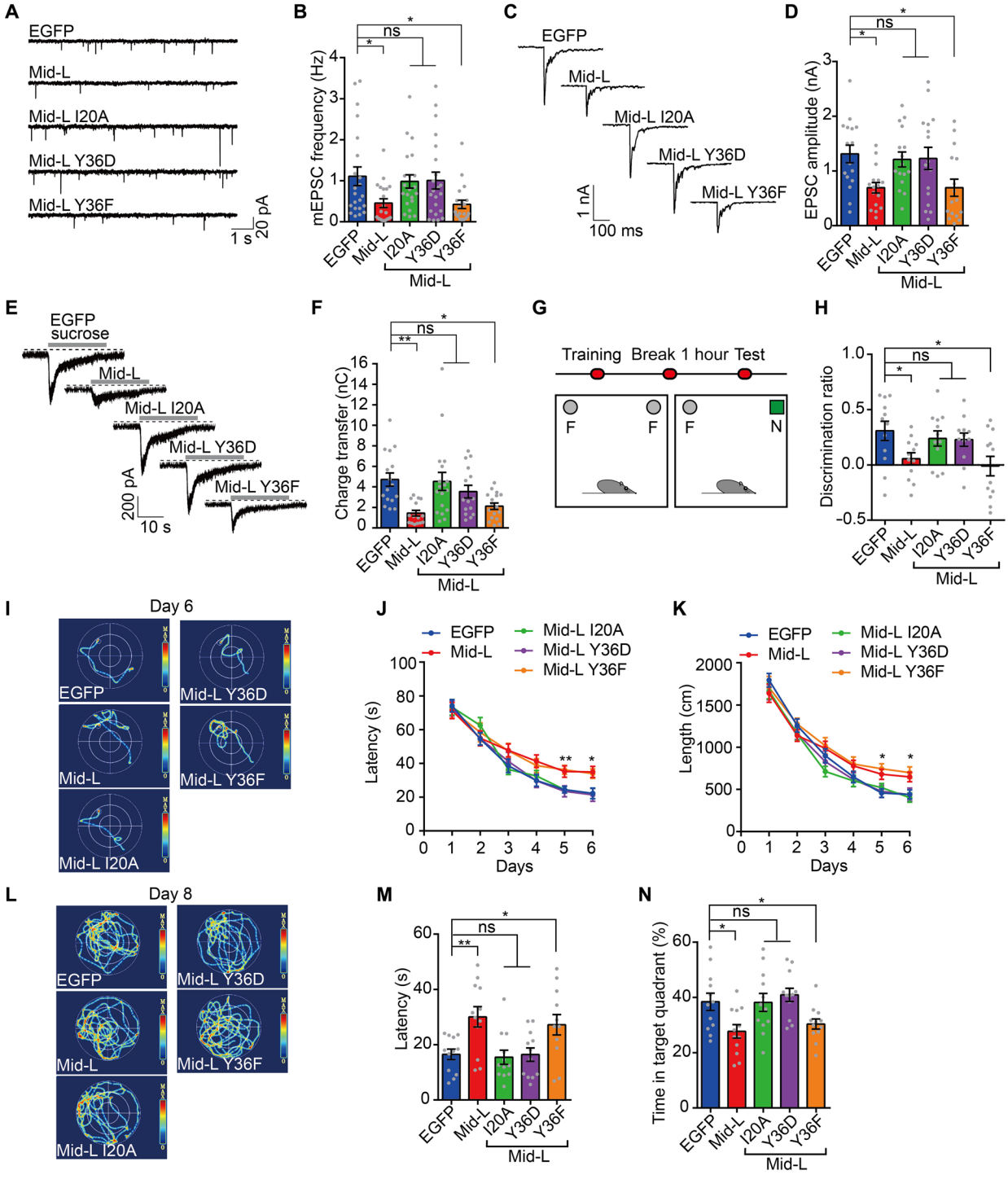

Fig. 6. Doc2-Munc13 interaction is critical for synaptic transmission and learning and memory. (**A** and **B**) Representative traces (A) and quantification of mEPSC frequency (B) in WT neurons expressing EGFP ($n = 22$), Mid-L ($n = 20$), Mid-L I20A ($n = 21$), Mid-L Y36D ($n = 22$), or Mid-L Y36F ($n = 20$). (**C** and **D**) Representative traces (C) and quantification of AP-evoked EPSC amplitude (D) in WT neurons expressing EGFP ($n = 16$), Mid-L ($n = 16$), Mid-L I20A ($n = 16$), Mid-L Y36D ($n = 16$), or Mid-L Y36F ($n = 16$). (**E** and **F**) Representative traces (E) and quantification of EPSCs evoked by 0.5 M sucrose (F) in WT neurons expressing EGFP ($n = 16$), Mid-L ($n = 15$), Mid-L I20A ($n = 18$), Mid-L Y36D ($n = 15$), or Mid-L Y36F ($n = 17$). (**G** and **H**) Schematic representation of the novel object recognition task (G) and quantification of the discrimination ratio of time (H). F, familiar object; N, novel object. (**I**) Representative hotspots of path tracings taken from training session at day 6 in Morris water maze test. (**J** and **K**) Average latency (J) and swim length (K) to reach a hidden platform plotted against the blocks of trials (days). (**L**) Representative hotspots of path tracings taken from the probe trial at day 8. (**M** and **N**) Quantification of the latency to reach the previously hidden platform area (M) and percentage of time spent in the target quadrant (N) on day 8. Data are presented as means ± SEM. For electrophysiological recordings, cells are from three independent experiments. For behavioral tests, 12 mice per group. Statistical significance and *P* values were determined by one-way ANOVA with Dunnett's multiple comparison test (*$P < 0.05$; **$P < 0.01$).

VAMP2 (fig. S7C). Furthermore, none of the mutants had any effect on the number of synapses (fig. S7D).

Next, we expressed Mid-L in the hippocampus of adult mice by using recombinant adeno-associated virus particles (rAAV2/9)–mediated gene expression system. We bilaterally applied the rAAV2/9-hSyn-Mid-L-EGFP into lateral ventricles to induce Mid-L expression throughout the hippocampus of adult mice (fig. S8, A and B). We next screened the function of Mid-L by using a large battery of the behavioral tests. In open-field test, compared to control mice (expression of EGFP), the total time spent in the center arena, total travel time, and distance spent in the open field were comparable in mice with expression of Mid-L or its mutants (fig. S8, C to F). We also carried out elevated plus maze test and found no significant differences in all groups (fig. S8, G to I). Together, the expression of Mid-L and its mutants in hippocampus produces no effect on the locomotion activity and emotional state.

We then conducted the novel object recognition test (Fig. 6G) and found that control mice spent more time exploring the novel object (Fig. 6H). In contrast, mice with expression of Mid-L or Mid-L Y36F had a significant reduction in the exploration discrimination ratio compared with those expressing Mid-L I20A or Mid-L Y36D (Fig. 6H). To examine learning and memory, we performed hidden-platform water maze test. During the learning acquisition phase, mice with expression of Mid-L or Mid-L Y36F significantly experienced longer latency and swim path length to reach the platform compared to control mice. In contrast, mice with expression of Mid-L I20A or Mid-L Y36D showed a similar ability to learn the task as control mice (Fig. 6, I to K). At the end of training, we removed the hidden platform in the maze and allowed mice to search the pool for 90 s. Again, mice expressing Mid-L or Mid-L Y36F, but not other groups, experienced longer latency for the first crossing to the platform region and spent shorter swimming time in the target quadrant (Fig. 6, L to N). Together, these results indicate that the interplay between Doc2 and Munc13 is critical for spatial learning and memory.

DISCUSSION

Our results lead to the following conclusions. First, the interaction between Doc2B and Munc13-1 involves a longer N-terminal sequence of Doc2B (residues 13 to 80, Mid-L) and the MUN domain of Munc13-1, which is predominantly mediated by a string of hydrophobic residues in the Mid-L and the NF hydrophobic pocket in the MUN domain, respectively. Second, this interaction promotes the corecruitment of Doc2B and Munc13-1 to the plasma membrane but instead inhibits Munc13-1 activity to initiate SNARE complex assembly and membrane fusion at the fusion sites. Third, EphB2 residing at the presynaptic membrane binds Doc2B and phosphorylates Doc2B at Y36, which dissociates Doc2B from Munc13-1 at the fusion sites, leading to Munc13-1–catalyzed SNARE complex assembly and membrane fusion. Fourth, EphB2-dependent phosphorylation of Doc2B, which modulates the association and dissociation between Doc2B and Munc13-1, is required for spontaneous release and synaptic augmentation. Fifth, elevation of Doc2B phosphorylation by increased EphrinB3-EphB2 signaling causes enhanced spontaneous release. Sixth, application of a Mid-L peptide that interferes with the spatiotemporal interplay between Doc2 and Munc13 impairs synaptic transmission and leads to dysfunction in spatial learning and memory in mice. Collectively, these results suggest a potential SAM-mediated retrograde signaling pathway where EphrinB3-EphB2 controls SNARE-dependent neurotransmitter release by modulating the interaction between Doc2 and Munc13 (Fig. 7).

Doc2 associates with Munc13 in vesicle tethering and replenishment

Doc2 and Munc13 are key components of the release machinery. Doc2 is particularly involved in spontaneous and asynchronous release, whereas Munc13 is fundamental for all types of release (*69*, *70*). At presynaptic terminals, Doc2 largely exists in the cytosol either in the free or vesicle-bound form (*34*) and is capable of moving to the plasma membrane dependent on its C_2 domain bound to Ca^{2+} (*29*, *45*). In contrast, Munc13-1, a member of the complex associated with tethering containing helical rods (CATCHER) family proteins (*71*, *72*), predominantly locates on the presynaptic membrane and serves as a central active zone element (*73*, *74*). Despite their distinct membrane-targeting behaviors, the interaction between Doc2 and Munc13 enables them to act interdependently. For instance, Munc13 recruits Doc2 to the plasma membrane upon PMA stimulation and (*37*, *40*), alternatively, Doc2 promotes Munc13 delivery to the plasma membrane in response to a rise in intracellular Ca^{2+} (*44*, *45*). This interaction, mediated by Mid-L and MUN, works in conjunction with multiple membrane-associating mechanisms mediated by the other domains of Doc2 and Munc13 [e.g., C_2A and C_2B of Doc2 (*30*, *31*) and C_2A (*22*–*24*), C_1-C_2B (*18*, *19*), and C_2C (*20, 21*) of Munc13]. This coordination is assumed to promote tethering of Doc2-bound vesicles to Munc13-riched fusion sites and/or accelerate the replenishment of both components at the fusion sites (Fig. 7). By these mechanisms, the fusion competence of Munc13 and Doc2 can be potentiated to meet the requirements of various activity-dependent release and plasticity.

The Mid sequence (residues 13 to 37) of Doc2 was previously identified as the region mediating Munc13 interaction. However, the exact binding sites between Doc2 and Munc13 have yet to be fully elucidated. Our biophysical results reveal that the interaction between Doc2 and Munc13 involves an extension of the Mid sequence (residues 13 to 80, Mid-L) of Doc2 and the NF pocket of Munc13 (Fig. 1). It is known that Syx1, which assumes a closed conformation bound to Munc18-1, represents a starting point for productive fusion pathway. In addition, both spontaneous and AP-evoked release requires Munc13 to catalyze the opening of Syx1, thereby initiating SNARE complex assembly (*75*). The NF pocket is exactly the catalytic site of Munc13 that opens Syx1. Here, our finding that the Doc2 Mid-L blocks the NF pocket to inhibit Munc13 activity in opening of Syx1 and SNARE complex assembly strongly suggests an inhibitory effect of Doc2 on Munc13-mediated vesicle priming (Fig. 2 and fig. S2). Consistently, introduction of the Doc2 Mid-L peptide significantly impairs synaptic transmission in cultured neurons and leads to abnormalities in learning and memory in adult mice (Fig. 6). Similarly, the inhibitory role of Doc2 Mid sequence overexpression was previously found in AP-evoked synaptic transmission in cholinergic synapses (*38*), PMA-induced synaptic potentiation in the calyx of Held (*37*), and dense-core vesicle exocytosis in PC12 cells (*76*). Moreover, the inhibitory role of Doc2 in vivo has also been supported in chromaffin cells (*41*, *77*). Together, Doc2 seems to exert a dual effect on Munc13 in a manner resembling that of Munc18-1 on Syx1. In our opinion, Doc2 and Munc18-1 not only serve as a chaperone to stabilize the conformation of Munc13 and Syx1 but function as a clamp to suppress the engagement of Munc13 and Syx1 in SNARE complex assembly, respectively. In this case, it is conceivable that the

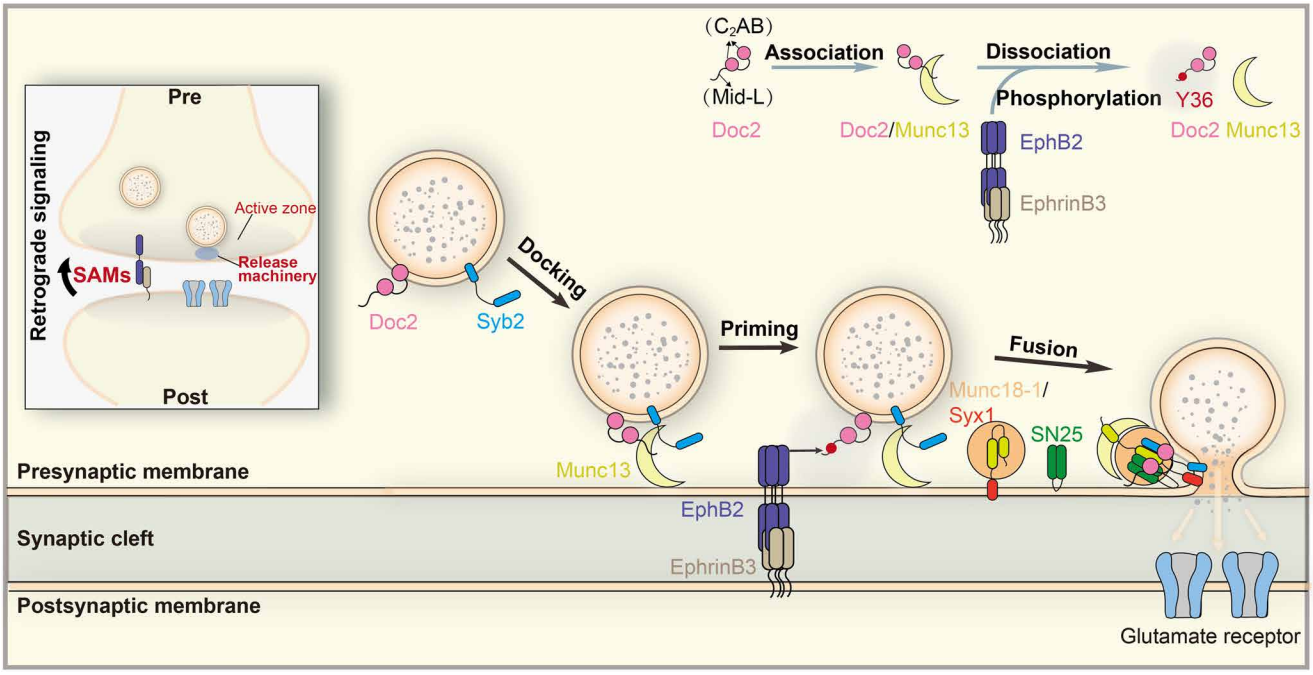

Fig. 7. Model of EphB2 retrograde signaling that modulates neurotransmitter release. Doc2 initially associates with vesicles via its C_2AB domain. In vesicle docking, Doc2 binds Munc13 via its Mid-L region, which mediates the association of Doc2-bound vesicles to Munc13-enriched fusion sites but renders vesicle priming by inhibiting SNARE complex assembly. In spontaneous release and/or synaptic augmentation, postsynaptic EphrinB3 clusters activate presynaptic EphB2, which causes Doc2 Mid-L (Y36) phosphorylation and the dissociation of Doc2 from Munc13 at the fusion sites. This dissociation promotes SNARE complex assembly and vesicle priming. Afterward, Doc2 C_2AB is capable of binding the plasma membrane (PS and PIP_2) and the assembled SNARE complex, and exerts its action to drive membrane fusion in response to Ca^{2+}.

tight association of Doc2 with Munc13 enables vesicle tethering close to the fusion sites and renders vesicles inaccessible to the priming stage, which collectively protects vesicles from occasionally fusing at the wrong place and at the wrong time (Fig. 7). Moreover, these results align well with previous observations in chromaffin cells that Doc2B synchronizes release via both positive and negative functions dependent on its Mid sequence (*41*).

Doc2 dissociates from Munc13 in vesicle priming and fusion

To achieve vesicle priming and fusion, neurons must evolve mechanisms to dissociate Doc2 from Munc13 at the fusion sites. In this study, we have identified EphB2, a SAM with tyrosine kinase activity, as a key factor that mediates dissociation of Doc2 from Munc13. Our identification that EphB2 positions close to the presynaptic elements, along with strong propensity to associate with the fusion machinery components including Munc13-1, Munc18-1, Syx1, and SN25, suggests a presynaptic mechanism of EphB2 (Fig. 3B and fig. S3C). Intriguingly, we observed that EphB2 displays strong ability to phosphorylate Doc2 at Y36 in the Mid-L region in vitro and in vivo via its tyrosine kinase domain (Fig. 3, H to N). This EphB2-dependent phosphorylation attenuates Doc2 binding with Munc13, thereby relieving the inhibitory effect of Doc2 on Munc13 activity in opening of Syx1 and SNARE complex assembly (Fig. 4). In our in vitro experimental conditions, the restoration of Munc13 activity is only partial, as evidenced by SNARE complex assembly and membrane fusion assays. A plausible explanation is that substituting Asp for the Tyr phosphorylation site (i.e., Y36D) may not accurately mimic the phosphorylated state of Doc2B, as Asp is singly charged, whereas pTyr is, nominally, doubly charged at physiological condition (*78*, *79*). Another possible explanation is that Y36 phosphorylation of Doc2B is not sufficient to fully dissociate Doc2B from Munc13, since the residues (i.e., amino acids 38 to 80) downstream of Y36 of Doc2B retain MUN interaction, which likely creates a steric hindrance effect that hinders Munc13-1 activity in opening Syx1. To examine the latter possibility, we tested Mid (residues 13 to 37) instead of Mid-L or Doc2B FL in our SNARE assembly assay and found that either Doc2B Mid Y36D or EphB2 treatment on Doc2B Mid led to a near-complete restoration of Munc13-catalyzed SNARE complex assembly (fig. S4, B and C). We suspect that under physiological conditions, some other Doc2 or Munc13 binding partners, such as Munc18, the SNARE proteins, and the membrane lipids, may help to relieve this steric hindrance effect to facilitate the dissociation of Doc2 from Munc13 (*3*, *34*, *80*–*82*). We also note that Doc2B phosphorylation at Y36 seems specific for EphB2 because EphA4 and other receptor or nonreceptor protein tyrosine kinases cannot directly phosphorylate Doc2 (fig. S3). In addition, Doc2B Y36 is conserved across species and its phosphorylation by EphB2 can also be observed in Doc2A as detected in vitro (fig. S5). Specifically, because of membrane localization and active zone association of EphB2, it is expected that efficient Doc2 phosphorylation should be restricted at the active zones after which the dissociation of Doc2 from Munc13 enables vesicle priming and fusion (Fig. 7).

Doc2 is implicated in spontaneous release, and this role was ascribed to an ability of its C_2AB domain that binds phospholipids and assembled SNARE complexes to promote membrane fusion in a Ca^{2+}-dependent manner (*30*, *31*). Here, our data suggest that in addition to C_2AB activity, Doc2 functions in spontaneous release in a manner requiring its sequential association and dissociation with

Munc13. Hence, Doc2 is assumed to support spontaneous release via the following sequential and coupled mechanisms: (i) association of Doc2 with Munc13 in the fusion sites to promote vesicle tethering, (ii) EphB2-dependent phosphorylation of Doc2 to relieve inhibition on Munc13-1 priming activity, and (iii) Ca^{2+}-regulated Doc2 actions (via C_2AB) on phospholipids and the SNARE complex for final membrane fusion.

An EphrinB3-EphB2–mediated retrograde signaling controls the release machinery

SAMs establish direct transsynaptic contact and mediate anterograde and retrograde signaling essential for information exchange at the synapse. Accumulating lines of evidence have indicated that multiple transsynaptic signaling mediated by Neurexin-Neuroligin, Ephrin-Eph, and N-cadherin can influence presynaptic structure and function in a retrograde manner. These mechanisms involve the alteration of many aspects of presynaptic elements' properties, but it remains largely unclear whether SAM-mediated retrograde signaling is able to control the presynaptic release machinery. Here, our results suggest an EphrinB3-EphB2–mediated retrograde signaling cascade that controls presynaptic SNARE complex assembly.

EphB2 was found to localize to both pre- and postsynaptic compartments and be involved in neuronal development, synaptic formation, and plasticity, mostly via a postsynaptic mechanism (*62*–*64*). In mature neurons, activation of postsynaptic EphB2 by EphrinBs promotes the recruitment and retention of N-methyl-d-aspartate receptors (NMDARs) and AMPA-type ionotropic glutamate receptors (AMPARs) at synapses and modulates the function of these glutamate receptors (*83*–*87*). Our results identified that stimulation of EphB2 by EphrinB3 enhances Doc2B phosphorylation in presynaptic compartment, resulting in increased spontaneous release (Figs. 3L and 5, E to G). This suggests that EphrinB3-EphB2 mediates a retrograde signaling to control release probability by modulating association and dissociation of the Doc2-Munc13 interaction. Furthermore, our results indicate that EphB2-dependent retrograde signaling pathway contributes to synaptic augmentation (Fig. 5, H to J), a type of short-term plasticity involved in learning and memory.

Neuronal activation enhances synaptic transmission by increasing both pre- and postsynaptic activity. In contrast to spontaneous activity with low Ca^{2+} levels, activation of presynaptic neurons (e.g., synaptic augmentation) leads to an elevation in intracellular Ca^{2+} levels. This increase in Ca^{2+} levels facilitates the recruitment of additional Doc2 and Munc13 molecules to the fusion sites, thereby enabling the fine-tuning of Doc2-Munc13 complex activities at these fusion sites. This fine-tuning can occur through the sensing of changes in DAG/PIP_2 levels on the plasma membrane and an increase in the phosphorylation level of EphB2. Thus, enhanced EphrinB3-EphB2 retrograde signaling modulates the interaction between Doc2 and Munc13 at the fusion sites, which increases the newly primed vesicles and potentiates their fusion competent required for activity-dependent presynaptic plasticity. Apart from EphB2-Doc2-Munc13 signaling cascade, it was previously found that EphB2 can phosphorylate Src family kinases (*88*). Src kinases are implicated in phosphorylating multiple presynaptic proteins, such as synaptophysin, synaptogyrin, synapsin, and Munc18-1 (*89*–*91*). Therefore, it is conceivable that EphB2 activates multiple downstream signaling pathways in presynaptic terminals that affect the release machinery. In postsynaptic neurons, as the ligand of EphB2, postsynaptic EphrinBs can modulate synaptic strength via mechanisms involving interaction with PSD-95 and AMPARs (*92*, *93*). In this regard, EphrinB connection to EphB2 beneficially couples the postsynaptic neurotransmitter receptors with the presynaptic release machinery, potentially forming a transsynaptic nanocolumn (*94*). Our findings will help to broaden our understanding of how SAM-mediated retrograde signaling regulates presynaptic structure and function.

MATERIALS AND METHODS

Antibodies

Rabbit polyclonal pY36 antibody, which recognizes residues 32 to 40 of Doc2B, was generated by ABclonal. The following antibodies were also used: rabbit polyclonal anti-Doc2B (1:3000; Proteintech, catalog no. 20574-1-AP, RRID: AB_10696316), mouse monoclonal anti-EphB2 (1:1000; Santa Cruz Biotechnology, catalog no. sc-130068, RRID: AB_2099958), rabbit polyclonal anti–Munc13-1 (1:2000; Proteintech, catalog no. 55053-1-AP, RRID: AB_10804173), rabbit polyclonal anti-PSD95 (1:3000; Abcam, catalog no. ab18258, RRID: AB_444362), rabbit polyclonal anti–Munc18-1 (1:2000; Proteintech, catalog no. 11459-1-AP, RRID: AB_2196690), rabbit polyclonal anti-SN25 (1:4000; Proteintech, catalog no. 14903-1-AP, RRID: AB_2192051), mouse monoclonal anti-Flag (1:200, catalog no. sc-166355, RRID: AB_2017593), rabbit polyclonal anti-Flag (1:2000; Proteintech, catalog no. 20543-1-AP, RRID: AB_11232216), rabbit polyclonal anti-VAMP2 (1:500; catalog no. 10135-1-AP, RRID: AB_256918), rabbit polyclonal anti-mCherry (1:3000; Proteintech, catalog no. 26765-1-AP, RRID: AB_2876881), mouse monoclonal anti-tubulin (1:4000; Proteintech, catalog no. 66031-1-Ig, RRID: AB_11042766), rabbit monoclonal anti-pTyr (1:2000; ABclonal, catalog no. AP116, RRID: AB_2864021), rabbit polyclonal anti-EGFP (1:3000; Proteintech, catalog no. 50430-2-AP, RRID: AB_11042881), rabbit polyclonal anti–RIM-1 (1:2000; Proteintech, catalog no. 24576-1-AP, RRID: AB_2879618), rabbit polyclonal anti-Syx1 (1:3000; Proteintech, catalog no. 15556-1-AP, RRID: AB_2198667), rabbit polyclonal anti-Syt1 (1:3000; Proteintech, catalog no. 14511-1-AP, RRID: AB_2199166), rabbit polyclonal anti-Syb2 (1:3000; Proteintech, catalog no. 10135-1-AP, RRID: AB_2256918), goat anti-mouse immunoglobulin G (IgG) (H+L), Alexa Fluor 488 (1:1000; Thermo Fisher Scientific, catalog no. A-11001, RRID: AB_2534069), goat anti-rabbit IgG (H+L), Alexa Fluor 546 (1:1000; Thermo Fisher Scientific, catalog no. A-11010, RRID: AB_2534077), rabbit monoclonal anti-EphB2 (1:500; Cell Signaling Technology, catalog no. 80329; RRID: AB_2800007), and rabbit monoclonal anti–IgG1-Fc (1:1000; Sino Biological, catalog no. 10702-R003).

Escherichia coli strain

Escherichia coli BL21 (DE3) cells were cultured in lysogeny broth medium at 37°C (for bacterial growth) or 16° to 25°C (for protein expression) as indicated at a shaking speed of 200 rpm.

HEK293 cell culture

HEK293 cells (American Type Culture Collection) were cultured in Dulbecco's modified Eagle's medium (DMEM; GIBCO) supplemented with 10% fetal bovine serum (GIBCO) and 1% penicillin-streptomycin (GIBCO) at 37°C in a cell incubator (Thermo Fisher Scientific) with 5% CO_2.

Primary cortical neuronal culture

Primary cortical neurons were derived from newborn *Doc2A*$^{+/+}$ or *Doc2A*$^{-/-}$ C57BL/6J P0 mouse pups. Glass coverslips coated with

poly-D-lysine (Sigma-Aldrich) were used to facilitate the attachment of the neurons. Cerebral cortex was dissociated with 0.25% trypsin-EDTA (GIBCO) and maintained in neurobasal complete medium (GIBCO) supplemented with 2% B27 (GIBCO), 200 μM L-glutamine (GIBCO), and 1% penicillin-streptomycin (GIBCO). The neurons were maintained in a cell incubator (Thermo Fisher Scientific) at 37°C with 5% CO_2 and replaced with fresh medium every 4 days. All animal procedures were approved by the institutional guidelines and the Animal Care and Use Committee of the animal core facility at Huazhong University of Science and Technology, Wuhan, China.

Mouse

Mice were bred and reared in accordance with institutional guidelines and the Animal Care and Use Committee of the animal core facility at Huazhong University of Science and Technology, Wuhan, China. Mice were housed in groups of five mice per cage under a 12-hour light-dark cycle, with lights on at 8:00 a.m., at a consistent ambient temperature (21° ± 1°C) and humidity (50 ± 5%).

For behavioral tests, WT mice (C57BL/6J, 8 weeks, male) were purchased from Charles River Laboratories, Beijing, China. All behavioral tests were conducted during the light phase of the cycle. For electrophysiological experiments, the *Doc2A*$^{-/-}$ mouse model (C57BL/6J) was made by Cyagen Biosciences Inc. by CRISPR-Cas–mediated genome engineering as demonstrated in fig. S6A. The *Doc2A* gene (National Center for Biotechnology Information reference sequence: NM_010069; Ensembl: ENSMUSG00000052301) is located on mouse chromosome 7. Specifically, the guide RNA (gRNA) sequences to deplete Doc2A are as follows: gRNA-A1, GTAGTCGGAGATCTGGCGGATGG; gRNA-A2, GCTGACGTACAGCGGGATCACGG; gRNA-B1, GGGTCCAGGGCACACGTTGATGG; gRNA-B2, AATGAGGAGCTGACGTACAGCGG. The 1064–base pair DNA fragment was depleted by these two gRNAs, which was confirmed by genotyping. Consequently, a frameshift occurred in the remaining portion of the Doc2A cDNA. mRNA level of Doc2A was totally depleted in exon 3, performed with primers 3F (GATGATACCACCGCCCTGGG) and 3R (TGGCCCTGAGGATTCTACAGTG). To avoid possible off-target editing of the genome, the mice were bred six generations with mice of C57BL/6J background before conducting any experiments.

Plasmids and protein purification

The coexpressed rats Munc18-1/Syx1 (residues 1 to 288) and Munc18-1/Syx1 (residues 1 to 261) were constructed into the pETDuet-1 vector (Novagen). The full-length rat Munc18-1 (residues 1 to 594), full-length rat Syb2 (residues 1 to 116), the cytoplasmic domain of Syb2 (residues 29 to 96) and Syb2 (residues 29 to 96, S61C), full-length SN25 (residues 1 to 203) and SN25 (residues 1 to 203, S187C), and the rat Syt1 cytoplasmic domain C_2AB (residues 140 to 421) were constructed into the pGEX-6p-1 vector (GE Healthcare). The cytoplasmic domain of rat Syx1 (residues 2 to 253) was cloned into the pGEX-KG vector. The rat Munc13-1 C_1C_2BMUN fragment (residues 529 to 1407, EF, 1453 to 1531) and C_1C_2BMUN (residues 529 to 1407, EF, 1453 to 1531, N1128A/F1131A) were cloned into the pFastBacHT B vector (Invitrogen). These proteins were expressed and purified as previously described (*12*).

The rat Munc13-1 MUN domain (residues 933 to 1407, EF, 1453 to 1531), fragments of the MUN, including MUN-ABC (residues 859 to 1407), MUN-BCD (residues 1011 to 1407, EF, 1453 to 1531), MUN-AB (residues 933 to 1167), MUN-BC (residues 1011 to 1407), and MUN-CD (residues 1148 to 1407, EF, 1453 to 1531), various point mutations within the MUN domain, and the human EphB2 kinase domain (residues 595 to 906) were all constructed into the pET-SUMO vector (Invitrogen), incorporating an N-terminal His_6 tag and SUMO tag. Cells were grown in LB media and induced with 0.4 mM isopropyl β-D-thiogalactoside (IPTG) at OD_{600} (optical density at 600 nm) of 0.6 to 0.8 for 20 hours at 18°C. Subsequently, the cells were harvested and lysed with AH-Nano Homogenize Machine (ATS Engineering Inc.) in buffer A [25 mM Hepes (pH 7.4), 150 mM KCl, 0.5% Triton X-100, and 1 mM phenylmethylsulfonyl fluoride (PMSF)]. The cell lysates were centrifuged at 16,000 rpm for 30 min using a JA-25.50 rotor (Beckman Coulter) at 4°C. The resulting supernatant was incubated with Ni^{2+}–nitrilotriacetic acid agarose (QIAGEN) at 4°C for 2 hours. The bound proteins were subsequently washed with buffer B [25 mM Hepes (pH 7.4) and 150 mM KCl] supplied with an additional 30 mM imidazole and finally eluted with 300 mM imidazole in buffer B. Last, the eluted proteins were cleaved by SUMO protease (10 U/mg protein) to remove SUMO tag at 4°C overnight and were further purified by size exclusion chromatography (GE Healthcare) in buffer B.

The full-length Doc2B (residues 1 to 412), full-length Doc2A (residues 1 to 405), and full-length Doc2C (residues 1 to 387) sequences were amplified from mouse brain cDNA library and cloned into the pGEX-6p-1 vector. In addition, the Doc2B fragments 1 to 37, 13 to 37, 13 to 60, 13 to 80, 13 to 120, 38 to 80, 38 to 412, and 1 to 80, and various Doc2B point mutations, the Doc2A fragments 12 to 36, 12 to 59, and 12 to 79, and various Doc2A point mutations, the Doc2C fragments 14 to 38, 14 to 61, and 14 to 81, and Munc13-1 MUN domain, were also constructed into the pGEX-6p-1 vector. The different fragments of Doc2A, Doc2B, and Doc2C, excluding Doc2B (38 to 412), were expressed in the *E. coli* BL21 (DE3) strain. The cells were cultured in LB media at 37°C until reaching an OD_{600} of 0.8 to 1.0. Subsequently, they were induced with 0.4 mM IPTG at 25°C for 12 hours. On the other hand, other recombinant proteins were induced with 0.4 mM IPTG at 18°C for 20 hours. Cells were lysed and broken in buffer C [25 mM Hepes (pH 7.4) and 1 M KCl] supplied with 0.5% Triton X-100, 5 mM EDTA, and 1 mM PMSF, and then centrifuged at 16,000 rpm for 30 min. The resulting supernatant was incubated with glutathione-Sepharose beads (2 ml, Amersham-Pharmacia Biotech) at 4°C for 3 hours. The bound proteins on the beads were washed with buffer C and then cleaved by GST-tagged PreScission protease (10 U/mg protein) at 4°C overnight in buffer B. The concentrations of Doc2B (1 to 80), Doc2B (13 to 37), Doc2B (13 to 80), and their respective mutations were determined by BCA Protein Assay Kit (Beyotime). For NMR spectroscopy, we used M9 minimal expression medium to produce uniformly $^{13}C/^{15}N$-labeled Doc2B (1 to 80). The medium was formulated with ammonium chloride (^{15}N, 99%, Cambridge Isotope Laboratories) as the sole nitrogen source (1 g/liter) and D-glucose (U-$^{13}C_6$, 99%, Cambridge Isotope Laboratories) as the sole carbon source (2 g/liter). For the purification of GST fusion protein, the bound proteins were washed with buffer C and then eluted by buffer B supplied with 20 mM L-glutathione (GSH; Amresco). Subsequently, all the eluted proteins were further purified by size exclusion chromatography.

For HEK293 translocation assays, Doc2B and Munc13-1 cDNA sequences were constructed into mCherry2-C1 (Addgene) and pEGFP-N3 (Clontech), respectively, in fig. S1D. For in vitro kinase assay in fig. S3A, Src (residues 258 to 535), Fyn (residues 260 to 537), Tec2 (residues 260 to 537), Fak2 (residues 412 to 692), TrkA (residues 500 to

799), and TrkB (residues 526 to 821) sequences were amplified from mouse brain cDNA library and cloned into the pEGFP-N3 vector. EGFR (residues 696 to 1022) and EphB2 (residues 595 to 906) were amplified from human brain cDNA library and cloned into the pEGFP-N3 vector. For immunoprecipitation experiments, human EphB2-Flag plasmid (residues 1 to 987) was a gift from C. Wang in Huazhong University of Science and Technology. In addition, mutant versions of EphB2, including EphB2-ΔSP (residues 1 to 885), EphB2-ΔKSP (residues 1 to 620), EphB2-KR, and EphB2-Y596E/Y602E were generated by site-directed mutagenesis. For neuron culture and virus infection assays, the sequences of Doc2A WT, Doc2B WT, as well as their respective mutant variants were inserted into pFHUUIG_shortU6 (L309) plasmid after the Ub promoter. The oligonucleotide sequences used for the acute knockdown were as follows: (CCTCAAGTACAGCTCACAGAA).

GST pull-down experiment

To monitor the interaction between Doc2 and Munc13-1, 3 μM GST or GST-tagged proteins were mixed with 4 μM indicated proteins. Afterward, the mixtures were loaded onto 10 μl of glutathione Sepharose 4B affinity beads (GE Healthcare) to a final volume of 300 μl with buffer B containing 0.01% Triton X-100 and 5 mM EDTA, and incubated at 4°C for 3 hours. To explore whether EphB2-dependent Doc2B phosphorylation attenuates Doc2B-MUN interaction (Fig. 4B), purified recombinant GST-Doc2 fragments were incubated with sumo-EphB2 kinase domain in 50 μl of reaction mixture containing 1 μM sumo-EphB2 kinase domain, 20 μM GST-Doc2 fragments, 100 μM ATP, 15 mM $MgCl_2$, and 5 mM dithiothreitol (DTT). Following incubation at 37°C for 30 min, the mixture was then combined with 4 μM MUN and loaded onto 10 μl of glutathione Sepharose 4B affinity beads (GE Healthcare) to a final volume of 300 μl with buffer B, and incubated at 4°C for 3 hours. After being extensively washed with the same buffer, the samples were boiled with SDS loading buffer at 100°C for 10 min, separated by SDS-PAGE, and detected by Coomassie Brilliant Blue (CBB) staining. Each experiment was repeated at least three times. Data were analyzed by ImageJ and Prism 8.0.0. For detecting Doc2B binding to EphB2 or Munc13-1 from brain samples, adult mouse brain was initially ground in buffer B supplied with 1% Triton X-100 and proteinase inhibitor cocktail (TargetMol) and then incubated with GST-Doc2B FL at 4°C overnight. The mixture was loaded onto glutathione Sepharose 4B affinity beads (GE Healthcare) at 4°C for 3 hours and subsequently washed with same buffer for four times. The samples were resolved by SDS-PAGE and analyzed by immunoblotting.

ITC assay

ITC assay was carried out on a MicroCal PEAQ-ITC (Malvern) at 25°C. All proteins used for ITC experiments were purified in an assay buffer D [25 mM Hepes (pH 7.4), 150 mM KCl, 5 mM EDTA, and 2 mM DTT]. Each titration point was performed by injecting a 2.2-μl aliquot of GST-tagged Doc2B from a syringe into the cell containing the MUN protein at a time interval of 2 min to ensure that the titration peak returned to the baseline. Titration data were analyzed using the MicroCal PEAQ-ITC analysis software and fitted with the one-site binding model.

NMR spectroscopy

NMR samples containing 0.18 mM of the uniformly $^{13}C/^{15}N$-labeled Doc2B (1 to 80), with and without the presence of 0.36 mM unlabeled MUN protein [called apo- and holo-Doc2B (1 to 80), respectively], were prepared in 25 mM Hepes (pH 7.4), 100 mM KCl, and 5% D_2O (v/v). All NMR spectra were acquired at 25°C on Bruker Avance III 850-MHz spectrometer equipped with a TCI cryogenic probe. 2D ^{1}H-^{15}N HSQC spectra were recorded for apo- and holo-Doc2B (1 to 80) samples. For backbone assignment, 3D HNCACB, CBCA(CO)NH, HNCA, HN(CO)CA, HNCO, and HN(CA)CO spectra were recorded for the apo-Doc2B (1 to 80) sample. Peak intensities were defined as calculated peak volumes by integration, and peak intensity ratio was defined as ratio between integrated peak volumes after (V) and before (V_0) addition of unlabeled MUN domain. NMR data were processed via NMRPipe program (https://doi.org/10.1007/BF00197809) and analyzed via POKY program (https://doi.org/10.1093/bioinformatics/btab180).

Analytical size exclusion chromatography

To detect the binding affinity between Doc2B and the MUN domain, 10 μM GST-Doc2B fragments and 10 μM MUN proteins were mixed in a total volume of 200 μl in buffer D. The mixtures were incubated for 2 hours at 4°C and then loaded onto a Superdex 200 Increase 10/300 GL size exclusion column preequilibrated with buffer D. Fractions were analyzed using SDS-PAGE followed by CBB staining.

Translocation assay

Translocation assay was performed as previously described upon PMA stimulation (*37*, *40*). Briefly, HEK293 cells were cultured in glass-bottom dishes (NEST) to reach 70 to 80% confluency. At this point, a mixture containing 1 μg of EGFP-tagged Munc13-1 and 1 μg of mCherry-tagged Doc2B was cotransfected into HEK293 cells using Lipofectamine 3000 (Invitrogen). Twenty-four hours after transfection, the HEK293 cells were treated with PMA at a final concentration of 0.1 μM and incubated at 37°C for 20 min. Images were acquired to analyze the plasma membrane localization of Doc2B and Munc13-1 by using a Nikon C2 confocal microscope equipped with a 60× oil-immersion objective.

Time-based FRET assay

Purified Syb2 (residues 29 to 96, S61C) and SN25 (residues 1 to 203, S187C) were separately mixed with 5× molar excess donor-dye BODIPY FL-maleimide (BDPY, Molecular Probes) and acceptor-dye tetramethylrhodamine-5-maleimide, single isomer (TMR, Molecular Probes) in buffer B and then gently rotated overnight at 4°C. After addition of 10 mM DTT to stop the labeling process, labeled proteins were further purified using PD-10 desalting columns (GE Healthcare) with buffer B to remove excess dyes. To monitor the effect of Doc2 on MUN-catalyzed SNARE complex assembly, 30 μM Doc2 proteins were incorporated into a mixture of 10 μM coexpressed Munc18-1/Syx1 (residues 1 to 261), 2 μM Syb2 S61C-BDPY, 10 μM SN25 S187C-TMR, and 30 μM MUN protein. To detect the effect of EphB2-dependent Doc2B Y36 phosphorylation on SNARE complex assembly, a preincubation step was conducted with 30 μM Doc2B and 5 μM EphB2 in a solution containing 100 μM ATP, 15 mM $MgCl_2$, and 5 mM DTT at 37°C for 30 min. Following this preincubation, the Doc2B-EphB2 mixture was added to the above reaction mixture. Time-based FRET assays were carried out with a high-temperature fluorescence microplate reader (Photon Technology Incorporated, Lawrenceville, NJ, USA; FluoDia T70). Donor fluorescence was monitored with an excitation wavelength of 485 nm and an emission wavelength of 513 nm at 30°C in 96-well plates. Decrease in donor fluorescence was calculated according to the following formula:

$E = (F_0 - F_{obs})/F_0$ (E, FRET efficiency; F_0, initial fluorescence intensity; F_{obs}, fluorescence intensity observed as a function time). Each experiment was repeated at least three times, and the data were analyzed by Prism 8.0.0 software.

Lipid-mixing experiment

The proteoliposomes reconstitution procedures were performed as previously described (*12*). Donor liposomes, which were reconstituted with Syb2 (residues 1 to 116), contained 60% palmitoyloleoylphosphatidylcholine (POPC), 17% palmitoyloleoylphosphatidylethanolamine (POPE), 20% dioleoyl-phosphatidylserine (DOPS), 1.5% N-(7-nitrobenz-2-oxa-1,3-diazol-4-yl) phosphatidylethanolamine (NBD-PE), and 1.5% rhodamine-PE. Acceptor liposomes, which were reconstituted with Munc18-1/Syx1 (residues 1 to 288), comprised 58% POPC, 15% POPE, 20% DOPS, 2% PIP_2, and 5% DAG. All lipid powders were purchased from Avanti Polar Lipids. The 5 mM lipid mixture was dried with nitrogen gas and applied with vacuum for at least 3 hours. Subsequently, the mixture was slowly resuspended with buffer B supplied with 2 mM DTT and 1% CHAPS (w/v, Amersco) and then vortexed for 15 min. Munc18-1/Syx1 (residues 1 to 288) and Syb2 (residues 1 to 116) were added to the mixture with a protein-to-lipid ratio of 1:500 and 1:1000, respectively. The protein-liposome mixtures were incubated at room temperature for 30 min and then dialyzed with Bio-Beads SM2 (1 g/liter, Bio-Rad) three times in buffer B to remove the detergent extensively. For lipid-mixing experiment, donor liposomes (0.25 mM total lipids) were mixed with acceptor liposomes (0.5 mM total lipids) in the presence of 5 μM SN25, 2 μM Syt1 C_2AB, 0.5 mM Ca^{2+}, 1.0 μM Munc13-1 (C_1C_2BMUN), and 1.0 μM Doc2B fragments in a total volume of 60 μl. All lipid-mixing assays were performed at 30°C and monitored donor (NBD: emission at 538 nm; excitation at 460 nm) fluorescence using a QM-40 spectrophotometer. Munc13-catalyzed lipid mixing was calculated by F_1/F_0 (F_1: the fluorescence intensity observed as a function time; F_0: the initial fluorescence intensity). Each experiment was repeated at least three times, and the data were analyzed by Prism 8.0.0 software.

Native-PAGE experiment

The Munc18-1/Syx1 complex was prepared by incubating Munc18-1 and Syx1 (residues 2 to 253) at a protein-to-protein ratio of 1.2:1 overnight at 4°C. To detect the effect of Doc2B on SNARE complex assembly, 30 μM Doc2B proteins were mixed with 3 μM/2.5 μM Munc18-1/Syx1, 10 μM Syb2, 10 μM SN25, and 30 μM MUN at 30°C for 3 hours in a total volume of 10 μl. Samples were mixed with native loading buffer and then added to the well of a 15% nondenaturing polyacrylamide gel (native gel). Next, electrophoresis was carried out with constant current 20 mA in a buffer containing 25 mM tris (pH 8.3) and 250 mM glycine at 4°C for 2 hours. After electrophoresis, the native gels were stained with CBB. Notably, the Munc18-1/Syx1 complex exhibited a sharp and clear band in the native gel.

Immunofluorescence

For monitoring the expression of Doc2B and EphB2 in hippocampus, paraffin-embedded brain slices were deparaffined, rehydrated, and placed in a repair box filled with EDTA antigen repair buffer (pH 8.0) in a microwave oven for antigen repair. After adding 5% bovine serum albumin (BSA) to block nonspecific binding for 30 min, slices were incubated with primary antibody (1:100) overnight at 4°C. Then, the sections were washed three times with phosphate-buffered saline (PBS; pH 7.4) in a Rocker device. Following incubation with secondary antibody (1:1000) at room temperature for 50 min in dark condition, the slices were slightly dried and the plate was sealed with antifluorescence quenching agent. Microscopy images were collected by digital scanner.

To detect the localization of EphB2 in presynaptic region and all variant of Doc2B rescue in electrophysiological experiments, primary hippocampus or cortical neurons were prepared from C57BL P0 mouse pups. Cultured cells were fixed in 4% paraformaldehyde and permeabilized with PBS containing 0.3% Triton X-100 for 10 min. Before incubation with primary antibody, samples were incubated with 5% BSA at room temperature for 1 hour to block nonspecific staining. After 3 hours of incubation with primary antibody at room temperature, the samples were washed three times with PBS and further stained with Alexa Fluor 488 goat anti-mouse and Alexa Fluor 546 goat anti-rabbit secondary antibodies (Molecular Probes).

To detect the binding of EphrinBs and EphB2, EGFP-EphB2–transfected HEK293 cells were incubated with preclustered EphrinB-Fc (human) (1 μg/ml) for 15 min. To facilitate preclustering, EphrinB1-Fc, EphrinB2-Fc, or EphrinB3-Fc fragments (Sino Biological) were mixed with recombinant anti–IgG1-Fc rabbit Antibody (Sino Biological) in a 1:2 ratio and incubated on ice for 1 hour. Cells were fixed and followed by staining with Alexa Fluor 546 goat anti-rabbit secondary antibody. Images were then acquired by a Nikon C2 confocal microscope equipped with a 60× oil-immersion objective. Identical settings were applied to all samples in each experiment.

Immunoblot and immunoprecipitation

HEK293 cells were cultured in DMEM media (GIBCO) supported by 10% fetal bovine serum (GIBCO) and 1% penicillin-streptomycin (GIBCO) at 37°C in cell incubator (Thermo Fisher Scientific) with 5% CO_2. When 70 to 80% confluency in 10-cm dishes was reached, HEK293 cells were transfected with various combinations of plasmids (10 μg/per plasmid) using Lipofectamine 3000 (Invitrogen). After 36 hours, the cells were harvested and lysed on ice in lysis buffer containing 50 mM tris (pH 7.5), 150 mM NaCl, 1% Triton X-100, 5 mM DTT, and protease inhibitor cocktail (TargetMol) for 30 min. Subsequently, the lysates were centrifuged at 14,000 rpm for 30 min to obtain clear lysates. For immunoprecipitation, cell lysates were incubated with 1 μg of antibody at 4°C overnight and then combined with rProtein G beads (Smart-Lifesciences) for 4 hours at 4°C. The beads were subsequently washed four times with lysis buffer, and the precipitates were eluted with 5× sample buffer. The eluted samples and whole-cell extracts were resolved on SDS-PAGE followed by immunoblotting with indicated antibodies.

Separation of pre- and postsynaptic elements

We separated pre- and postsynaptic elements as previously described (*61*). First, we isolated synaptosomes with Ficoll discontinuous gradient centrifugation. The brain tissues were placed into ice-cold sucrose buffer [320 mM sucrose and 5 mM Hepes (pH 7.4)] and gently ground for 1 min. After centrifuging the brain homogenate at 1000*g* for 10 min, the supernatant was carefully removed, and the resulting pellet was dissolved in sucrose buffer to obtain the S1 fraction. The S1 fraction was then centrifuged at 15,000*g* for 15 min. Upon removing the supernatant, it was observed that the cortical (soft) portion of the pellet in the resulting P2 fraction tended to detach. P2 fraction (0.5 ml) was pipetted onto the top of discontinuous gradient [13% 2 ml, 9% 0.5 ml, 5% 2 ml Ficoll (w/v) in sucrose buffer] and centrifuged at 26,700 rpm for 35 min at 4°C (Beckman SW55Ti). Synaptosomes

were obtained by slowly and carefully pipetting the 9% Ficoll fraction and diluting it with sodium buffer [containing 10 mM glucose, 5 mM KCl, 140 mM NaCl, 5 mM $NaHCO_3$, 1 mM $MgCl_2$, 1.2 mM Na_2HPO_4, and 20 mM Hepes (pH 7.4)].

Next, we separated presynaptic, postsynaptic, and extrajunctional synaptic proteins. One milliliter of synaptosome components was diluted and resuspended in 5 ml of 0.1 mM $CaCl_2$. An equal volume of 2× solubilization buffer [20 mM tris (pH 6.0) and 1% Triton X-100] was added to the mixture and then incubated on ice for 50 min. After centrifugation at 40,000*g* for 30 min at 4°C, the resulting supernatant contained the extrasynaptic component, while the pellet contained the synaptic junction complex. The pellet obtained earlier was resuspended in 10 ml of 1× solubilization buffer with a pH of 8.0 and incubated on ice for 50 min. Following this, the samples were centrifuged at 40,000*g* for 30 min at 4°C. The resulting supernatant was identified as the presynaptic component, while the pellet contained the postsynaptic component. To increase their concentration, the extrasynaptic component and presynaptic component were then precipitated by trichloroacetic acid.

In vitro kinase assay

For in vitro phosphorylation, purified recombinant GST-Doc2 fragments were incubated with sumo-EphB2 kinase domain in a 50-μl reaction mixture containing 0.5 μM sumo-EphB2 kinase domain, 5 μM GST-Doc2 fragments, 100 μM ATP, 15 mM $MgCl_2$, and 5 mM DTT. After incubating at 37°C for 30 min, the reaction was terminated by the addition of 13 μl of 5× SDS loading buffer. For phosphorylation in HEK293 cells, cells were transfected as indicated, followed by lysing with lysis buffer containing 50 mM tris (pH 7.5), 150 mM NaCl, 1% Triton X-100, 5 mM DTT, protease inhibitor cocktail (TargetMol), and phosphatase inhibitor cocktail (TargetMol) for 30 min. Cell lysates were incubated with 1 μg of antibody at 4°C overnight and then combined with rProtein G beads (Smart-Lifesciences) for 2 hours at 4°C. Next, the beads were washed four times with lysis buffer and the pellet was eluted with 5× sample buffer. For fig. S3A, following the washing step, 20 μM GST-Doc2 Mid was incubated with purified beads in a 50 μl of reaction mixture at 37°C for 30 min. For phosphorylation in cultured neurons, before harvest and lysis, the cells were incubated with preclustered EphirnB3-Fc (2 μg/ml) for 20 min at 37°C. The pellet was resolved by SDS-PAGE and subjected to Western blot analysis by indicated antibody.

Lentivirus preparation

Lentivirus preparation was performed as described before (*95*). To prepare lentivirus viral particles, six-well dishes of HEK293 cells with 70 to 80% confluence were transfected with 1.5 μg of L309 containing Doc2B mutants along with helper plasmids at a ratio of L309:VSVG:RRE:REV = 3:1:2:2. After 4 to 6 hours of transfection, HEK293 cells were replaced with fresh medium and incubated for an additional 48 hours. To concentrate the virus, the medium was harvested and concentrated by sucrose-gradient centrifugation. Following the centrifugation step, the virus particles were resuspended with PBS at 4°C overnight. Neurons at days in vitro (DIV) 7 to 8 were then infected with virus, and electrophysiological recordings were performed at DIV12 to DIV13.

Electrophysiological recordings

Electrophysiological recordings were performed as described before (*14*, *40*). In brief, whole-cell patch-clamp was performed by using an amplifier (HEKA EPC10). Borosilicate glass capillary tubes (Sutter) were pulled into patch pipettes, with resistances ranging from 3 to 5 megohms, using a P-97 pipette puller (Sutter). The whole-cell pipette solution was composed of 120 mM CsCl, 10 mM Hepes, 10 mM EGTA, 0.3 mM Na-guanosine triphosphate, and 3 mM Mg-ATP (pH 7.2, adjusted with CsOH). The neuron bath solution contained 140 mM NaCl, 5 mM KCl, 2 mM $MgCl_2$, 2 mM $CaCl_2$, 10 mM Hepes, and 10 mM glucose (pH 7.4). mEPSCs were recorded by amplifier at a holding potential of −70 mV in the presence of tetrodotoxin (1 μM) to block APs and picrotoxin (PTX; 50 μM) to pharmacologically isolate inhibitory postsynaptic currents (IPSCs). To record the evoked EPSCs, QX-314 was added into pipette solution and PTX was applied in bath solution to pharmacologically isolate IPSCs. Neurons were stimulated with 100 μA for 1 ms. The RRP size was measured by application of hypertonic sucrose (0.5 M). The data were digitized at 10 kHz with a 2-kHz low-pass filter. The EPSC currents were analyzed by Clampfit 10 (Molecular Devices).

Augmentation was induced by a stimulus train at 10 Hz for 5 s. Evoked EPSCs was recorded at 0.2 Hz for 30 s before stimulation and 45 s after stimulation. EphrinB3-induced mEPSC increase was performed by replacing basal bath solution with EphrinB3-containing bath solution. A baseline was recorded for at least 10 min before EphrinB3 treatment, and EphrinB3-induced mEPSC were recorded for 50 min.

Stereotaxic injection

Mice (C57BL/6J, 8 weeks, male) were anesthetized with isoflurane (2%, RWD) and placed in a stereotaxic apparatus. After the head was fixed, the skull was exposed, and burr holes were made; a microsyringe (World Precision Instruments) was slowly lowered into the lateral ventricles at 0.34 mm anteroposterior, 1.0 mm mediolateral, and 2.25 mm dorsoventral relative to bregma. AAV containing Mid-L or its mutations (Brain Case, 1 μl) was pressure-injected into each hemisphere. The syringe was kept still for 5 min until slowly retracted. After suture, the mice were placed on a heating pad to recover from anesthesia. The behavior experiments were conducted 4 weeks after the virus injection.

Behavioral tests

The mice were tested in the open field, followed by the novel object recognition task, then the elevated plus maze, and finally the Morris water maze.

Open field

Spontaneous locomotor activity in an open field was measured in a rectangular Plexiglas box (50 cm by 50 cm by 50 cm) comprising four walls and an open roof. Experiments were performed in quiet conditions. Animals were placed in the center of the bottom area and were individually tested in one 5-min session. Each subject was introduced to the apparatus by placing them near the center of arena, allowing the mice to explore the apparatus for 5 min. Before each subject was tested, the inner wall and bottom surface of the square box were cleaned with 75% ethanol to avoid any residual information. The movement of the mouse was video-tracked and analyzed.

Novel object recognition

Mice were transferred to the test room and acclimated for at least 1 hour before test. The test was performed in a rectangular Plexiglas box (50 cm by 50 cm by 50 cm) under a white light. On day 1, mice were placed in the test arena and allowed to explore freely for 10 min. On day 2, each mouse was presented with two identical objects in the same chamber and allowed to explore freely for 5 min. One hour after

this training session, the mice were placed back into the same arena for the test session. During the test session, the mice were exposed to a novel object of different shape and texture, as well as the familiar object used during training. The arenas and objects were cleaned with 75% ethanol between each test. Behavior was recorded with a video tracking system. Time spent exploring each object was recorded for subsequent data analysis. Discrimination ratio was calculated according to the following formula: $D = (A - B)/(A + B)$ (D, discrimination ration; A, time mice spent exploring a novel object during a 5-min test session; B, time mice spent exploring a familiar object during a 5-min test session).

Elevated pulse maze

The elevated plus maze was made of two open arms and two enclosed arms with 15-cm-high walls on each side, elevated 60 cm above the ground. During the test session, mice were placed at the junction between the open and closed arms and allowed to explore freely for 5 min. The maze was cleaned thoroughly with 75% ethanol between each test. Total distance traveled and time spent in both the open and closed arms were calculated for data analysis.

Morris water maze

The maze consists of a circular pool with a diameter of 120 cm, filled with water at a temperature of 21° ± 2°C. The water is made opaque by addition of white milk powder; within the pool is a hidden platform with a diameter of 6 cm, positioned 1 cm below the surface of the water. Before the test, the mice were allowed to acclimate to test room for at least 1 hour. During the training trials, the mice were trained to find the invisible platform within 90 s on six consecutive days with three trials per day. Each training interval was 1 hour. If the mice failed to find the platform within 90 s, we guided them to the platform and allowed to stay for 15 s to acclimate the distinct extra-maze cues on the walls. Escape latency to find the hidden platform and path length were recorded. After 24 hours of rest, the platform was removed and mice were individually set float to search the pool for 90 s (probe tests). Then, the time spent in each quadrant was analyzed.

Supplementary Materials

This PDF file includes:

Figs. S1 to S8
Table S1
Legends for data S1 and S2

Other Supplementary Material for this manuscript includes the following:

Data S1 and S2

REFERENCES AND NOTES

1. T. C. Südhof, Neurotransmitter release: The last millisecond in the life of a synaptic vesicle. *Neuron* **80**, 675–690 (2013).
2. A. T. Brunger, U. B. Choi, Y. Lai, J. Leitz, Q. Zhou, Molecular mechanisms of fast neurotransmitter release. *Annu. Rev. Biophys.* **47**, 469–497 (2018).
3. J. Rizo, Molecular mechanisms underlying neurotransmitter release. *Annu. Rev. Biophys.* **51**, 377–408 (2022).
4. R. B. Sutton, D. Fasshauer, R. Jahn, A. T. Brunger, Crystal structure of a SNARE complex involved in synaptic exocytosis at 2.4 A resolution. *Nature* **395**, 347–353 (1998).
5. T. Weber, B. V. Zemelman, J. A. McNew, B. Westermann, M. Gmachl, F. Parlati, T. H. Söllner, J. E. Rothman, SNAREpins: Minimal machinery for membrane fusion. *Cell* **92**, 759–772 (1998).
6. R. Jahn, D. Fasshauer, Molecular machines governing exocytosis of synaptic vesicles. *Nature* **490**, 201–207 (2012).
7. R. F. Toonen, O. Kochubey, H. de Wit, A. Gulyas-Kovacs, B. Konijnenburg, J. B. Sørensen, J. Klingauf, M. Verhage, Dissecting docking and tethering of secretory vesicles at the target membrane. *EMBO J.* **25**, 3725–3737 (2006).
8. I. Dulubova, S. Sugita, S. Hill, M. Hosaka, I. Fernandez, T. C. Südhof, J. Rizo, A conformational switch in syntaxin during exocytosis: Role of munc18. *EMBO J.* **18**, 4372–4382 (1999).
9. F. Varoqueaux, A. Sigler, J. S. Rhee, N. Brose, C. Enk, K. Reim, C. Rosenmund, Total arrest of spontaneous and evoked synaptic transmission but normal synaptogenesis in the absence of Munc13-mediated vesicle priming. *Proc. Natl. Acad. Sci. U.S.A.* **99**, 9037–9042 (2002).
10. C. Imig, S. W. Min, S. Krinner, M. Arancillo, C. Rosenmund, T. C. Südhof, J. Rhee, N. Brose, B. H. Cooper, The morphological and molecular nature of synaptic vesicle priming at presynaptic active zones. *Neuron* **84**, 416–431 (2014).
11. C. Ma, W. Li, Y. Xu, J. Rizo, Munc13 mediates the transition from the closed syntaxin-Munc18 complex to the SNARE complex. *Nat. Struct. Mol. Biol.* **18**, 542–549 (2011).
12. X. Yang, S. Wang, Y. Sheng, M. Zhang, W. Zou, L. Wu, L. Kang, J. Rizo, R. Zhang, T. Xu, C. Ma, Syntaxin opening by the MUN domain underlies the function of Munc13 in synaptic-vesicle priming. *Nat. Struct. Mol. Biol.* **22**, 547–554 (2015).
13. S. Wang, U. B. Choi, J. Gong, X. Yang, Y. Li, A. L. Wang, X. Yang, A. T. Brunger, C. Ma, Conformational change of syntaxin linker region induced by Munc13s initiates SNARE complex formation in synaptic exocytosis. *EMBO J.* **36**, 816–829 (2017).
14. X. Wang, J. Gong, L. Zhu, S. Wang, X. Yang, Y. Xu, X. Yang, C. Ma, Munc13 activates the Munc18-1/syntaxin-1 complex and enables Munc18-1 to prime SNARE assembly. *EMBO J.* **39**, e103631 (2020).
15. T. Shu, H. Jin, J. E. Rothman, Y. Zhang, Munc13-1 MUN domain and Munc18-1 cooperatively chaperone SNARE assembly through a tetrameric complex. *Proc. Natl. Acad. Sci. U.S.A.* **117**, 1036–1041 (2020).
16. Y. Lai, U. B. Choi, J. Leitz, H. J. Rhee, C. Lee, B. Altas, M. Zhao, R. A. Pfuetzner, A. L. Wang, N. Brose, J. Rhee, A. T. Brunger, Molecular mechanisms of synaptic vesicle priming by Munc13 and Munc18. *Neuron* **95**, 591–607.e10 (2017).
17. K. P. Stepien, J. Xu, X. Zhang, X.-C. Bai, J. Rizo, SNARE assembly enlightened by cryo-EM structures of a synaptobrevin–Munc18-1–syntaxin-1 complex. *Sci. Adv.* **8**, eabo5272 (2022).
18. J. Xu, M. Camacho, Y. Xu, V. Esser, X. Liu, T. Trimbuch, Y.-Z. Pan, C. Ma, D. R. Tomchick, C. Rosenmund, J. Rizo, Mechanistic insights into neurotransmitter release and presynaptic plasticity from the crystal structure of Munc13-1 C1C2BMUN. *eLife* **6**, e22567 (2017).
19. F. Michelassi, H. Liu, Z. Hu, J. S. Dittman, A C1–C2 module in Munc13 inhibits calcium-dependent neurotransmitter release. *Neuron* **95**, 577–590.e5 (2017).
20. B. Quade, M. Camacho, X. Zhao, M. Orlando, T. Trimbuch, J. Xu, W. Li, D. Nicastro, C. Rosenmund, J. Rizo, Membrane bridging by Munc13-1 is crucial for neurotransmitter release. *eLife* **8**, e42806 (2019).
21. K. Grushin, R. V. Kalyana Sundaram, C. V. Sindelar, J. E. Rothman, Munc13 structural transitions and oligomers that may choreograph successive stages in vesicle priming for neurotransmitter release. *Proc. Natl. Acad. Sci. U.S.A.* **119**, e2121259119 (2022).
22. L. Deng, P. S. Kaeser, W. Xu, T. C. Südhof, RIM proteins activate vesicle priming by reversing autoinhibitory homodimerization of Munc13. *Neuron* **69**, 317–331 (2011).
23. J. Lu, M. Machius, I. Dulubova, H. Dai, T. C. Südhof, D. R. Tomchick, J. Rizo, Structural basis for a Munc13-1 homodimer to Munc13-1/RIM heterodimer switch. *PLOS Biol.* **4**, e192 (2006).
24. M. Camacho, J. Basu, T. Trimbuch, S. Chang, C. Pulido-Lozano, S.-S. Chang, I. Duluvova, M. Abo-Rady, J. Rizo, C. Rosenmund, Heterodimerization of Munc13 C2A domain with RIM regulates synaptic vesicle docking and priming. *Nat. Commun.* **8**, 15293 (2017).
25. N. Lipstein, T. Sakaba, B. H. Cooper, K. H. Lin, N. Strenzke, U. Ashery, J.-S. Rhee, H. Taschenberger, E. Neher, N. Brose, Dynamic control of synaptic vesicle replenishment and short-term plasticity by Ca^{2+}-calmodulin-Munc13-1 signaling. *Neuron* **79**, 82–96 (2013).
26. J. Xu, T. Mashimo, T. C. Südhof, Synaptotagmin-1, -2, and -9: Ca^{2+} sensors for fast release that specify distinct presynaptic properties in subsets of neurons. *Neuron* **54**, 567–581 (2007).
27. S. Orita, T. Sasaki, A. Naito, R. Komuro, T. Ohtsuka, M. Maeda, H. Suzuki, H. Igarashi, Y. Takai, Doc2: A novel brain protein having two repeated C_2-like domains. *Biochem. Biophys. Res. Commun.* **206**, 439–448 (1995).
28. G. Sakaguchi, S. Orita, M. Maeda, H. Igarashi, Y. Takai, Molecular cloning of an isoform of Doc2 having C2-like domains. *Biochem. Biophys. Res. Commun.* **217**, 1053–1061 (1995).
29. A. J. Groffen, R. Friedrich, E. C. Brian, U. Ashery, M. Verhage, DOC2A and DOC2B are sensors for neuronal activity with unique calcium-dependent and kinetic properties. *J. Neurochem.* **97**, 818–833 (2006).
30. J. Yao, J. D. Gaffaney, S. E. Kwon, E. R. Chapman, Doc2 is a Ca^{2+} sensor required for asynchronous neurotransmitter release. *Cell* **147**, 666–677 (2011).
31. A. J. Groffen, S. Martens, R. Diez Arazola, L. N. Cornelisse, N. Lozovaya, A. P. de Jong, N. A. Goriounova, R. L. Habets, Y. Takai, J. G. Borst, N. Brose, H. T. McMahon, M. Verhage, Doc2b is a high-affinity Ca^{2+} sensor for spontaneous neurotransmitter release. *Science* **327**, 1614–1618 (2010).
32. Z. P. Pang, T. Bacaj, X. Yang, P. Zhou, W. Xu, T. C. Südhof, Doc2 supports spontaneous synaptic transmission by a Ca^{2+}-independent mechanism. *Neuron* **70**, 244–251 (2011).
33. N. A. Courtney, J. S. Briguglio, M. M. Bradberry, C. Greer, E. R. Chapman, Excitatory and inhibitory neurons utilize different Ca^{2+} sensors and sources to regulate spontaneous release. *Neuron* **98**, 977–991.e5 (2018).

34. M. Verhage, K. J. de Vries, H. Røshol, J. P. Burbach, W. H. Gispen, T. C. Südhof, DOC2 proteins in rat brain: Complementary distribution and proposed function as vesicular adapter proteins in early stages of secretion. *Neuron* **18**, 453–461 (1997).
35. N. Korteweg, F. A. Denekamp, M. Verhage, J. P. Burbach, Different spatiotemporal expression of DOC2 genes in the developing rat brain argues for an additional, nonsynaptic role of DOC2B in early development. *Eur. J. Neurosci.* **12**, 165–171 (2000).
36. S. Orita, A. Naito, G. Sakaguchi, M. Maeda, H. Igarashi, T. Sasaki, Y. Takai, Physical and functional interactions of Doc2 and Munc13 in Ca^{2+}–dependent exocytotic machinery. *J. Biol. Chem.* **272**, 16081–16084 (1997).
37. R. R. Duncan, A. Betz, M. J. Shipston, N. Brose, R. H. Chow, Transient, phorbol ester-induced DOC2-Munc13 interactions *in vivo*. *J. Biol. Chem.* **274**, 27347–27350 (1999).
38. S. Mochida, S. Orita, G. Sakaguchi, T. Sasaki, Y. Takai, Role of the Doc2α–Munc13–1 interaction in the neurotransmitter release process. *Proc. Natl. Acad. Sci. U.S.A.* **95**, 11418–11422 (1998).
39. T. Hori, Y. Takai, T. Takahashi, Presynaptic mechanism for phorbol ester-induced synaptic potentiation. *J. Neurosci.* **19**, 7262–7267 (1999).
40. R. Xue, D. A. Ruhl, J. S. Briguglio, A. G. Figueroa, R. A. Pearce, E. R. Chapman, Doc2-mediated superpriming supports synaptic augmentation. *Proc. Natl. Acad. Sci. U.S.A.* **115**, E5605–E5613 (2018).
41. S. Houy, A. J. Groffen, I. Ziomkiewicz, M. Verhage, P. S. Pinheiro, J. B. Sørensen, Doc2B acts as a calcium sensor for vesicle priming requiring synaptotagmin-1, Munc13-2 and SNAREs. *eLife* **6**, e27000 (2017).
42. S. Orita, T. Sasaki, R. Komuro, G. Sakaguchi, M. Maeda, H. Igarashi, Y. Takai, Doc2 enhances Ca^{2+}–dependent exocytosis from PC12 cells. *J. Biol. Chem.* **271**, 7257–7260 (1996).
43. S. Orita, T. Sasaki, Y. Takai, 10 - Doc2α as modulator of Ca^{2+}-dependent exocytosis. *Methods Enzymol.* **329**, 83–90 (2001).
44. R. Friedrich, I. Gottfried, U. Ashery, Munc13-1 translocates to the plasma membrane in a Doc2B- and calcium-dependent manner. *Front. Endocrinol. (Lausanne)* **4**, 119 (2013).
45. A. J. Groffen, E. C. Brian, J. J. Dudok, J. Kampmeijer, R. F. Toonen, M. Verhage, Ca^{2+}-induced recruitment of the secretory vesicle protein DOC2B to the target membrane. *J. Biol. Chem.* **279**, 23740–23747 (2004).
46. H. W. Tao, M. Poo, Retrograde signaling at central synapses. *Proc. Natl. Acad. Sci. U.S.A.* **98**, 11009–11015 (2001).
47. W. G. Regehr, M. R. Carey, A. R. Best, Activity-dependent regulation of synapses by retrograde messengers. *Neuron* **63**, 154–170 (2009).
48. K. J. Iremonger, J. I. Wamsteeker Cusulin, J. S. Bains, Changing the tune: Plasticity and adaptation of retrograde signals. *Trends Neurosci.* **36**, 471–479 (2013).
49. K. Futai, M. J. Kim, T. Hashikawa, P. Scheiffele, M. Sheng, Y. Hayashi, Retrograde modulation of presynaptic release probability through signaling mediated by PSD-95-neuroligin. *Nat. Neurosci.* **10**, 186–195 (2007).
50. B. K. Lim, N. Matsuda, M.-M. Poo, Ephrin-B reverse signaling promotes structural and functional synaptic maturation *in vivo*. *Nat. Neurosci.* **11**, 160–169 (2008).
51. N. Vitureira, M. Letellier, I. J. White, Y. Goda, Differential control of presynaptic efficacy by postsynaptic N-cadherin and β-catenin. *Nat. Neurosci.* **15**, 81–89 (2011).
52. X.-J. Tong, E. J. López-Soto, L. Li, H. Liu, D. Nedelcu, D. Lipscombe, Z. Hu, J. M. Kaplan, Retrograde synaptic inhibition is mediated by α-neurexin binding to the α2δ subunits of N-type calcium channels. *Neuron* **95**, 326, 340.e5 (2017).
53. N.-J. Xu, M. Henkemeyer, Ephrin-B3 reverse signaling through Grb4 and cytoskeletal regulators mediates axon pruning. *Nat. Neurosci.* **12**, 268–276 (2009).
54. A. Stan, K. N. Pielarski, T. Brigadski, N. Wittenmayer, O. Fedorchenko, A. Gohla, V. Lessmann, T. Dresbach, K. Gottmann, Essential cooperation of N-cadherin and neuroligin-1 in the transsynaptic control of vesicle accumulation. *Proc. Natl. Acad. Sci. U.S.A.* **107**, 11116–11121 (2010).
55. J. S. Polepalli, H. Wu, D. Goswami, C. H. Halpern, T. C. Südhof, R. C. Malenka, Modulation of excitation on parvalbumin interneurons by neuroligin-3 regulates the hippocampal network. *Nat. Neurosci.* **20**, 219–229 (2017).
56. S. Wang, Y. Li, J. Gong, S. Ye, X. Yang, R. Zhang, C. Ma, Munc18 and Munc13 serve as a functional template to orchestrate neuronal SNARE complex assembly. *Nat. Commun.* **10**, 69 (2019).
57. A. R. Boxall, B. Lancaster, Tyrosine kinases and synaptic transmission. *Eur. J. Neurosci.* **10**, 2–7 (1998).
58. A. L. Purcell, T. J. Carew, Tyrosine kinases, synaptic plasticity and memory: Insights from vertebrates and invertebrates. *Trends Neurosci.* **26**, 625–630 (2003).
59. D. J. Liebl, C. J. Morris, M. Henkemeyer, L. F. Parada, mRNA expression of ephrins and Eph receptor tyrosine kinases in the neonatal and adult mouse central nervous system. *J. Neurosci. Res.* **71**, 7–22 (2003).
60. M. S. Kayser, M. J. Nolt, M. B. Dalva, EphB receptors couple dendritic filopodia motility to synapse formation. *Neuron* **59**, 56–69 (2008).
61. D. Bouvier, A. T. Corera, M.-E. Tremblay, M. Riad, M. Chagnon, K. K. Murai, E. B. Pasquale, E. A. Fon, G. Doucet, Pre-synaptic and post-synaptic localization of EphA4 and EphB2 in adult mouse forebrain. *J. Neurochem.* **106**, 682–695 (2008).
62. R. Klein, Bidirectional modulation of synaptic functions by Eph/ephrin signaling. *Nat. Neurosci.* **12**, 15–20 (2009).
63. S. Sloniowski, I. M. Ethell, Looking forward to EphB signaling in synapses. *Semin. Cell Dev. Biol.* **23**, 75–82 (2012).
64. H. R. Washburn, P. Chander, K. D. Srikanth, M. B. Dalva, Transsynaptic signaling of ephs in synaptic development, plasticity, and disease. *Neuroscience* **508**, 137–152 (2023).
65. M. Hruska, M. B. Dalva, Ephrin regulation of synapse formation, function and plasticity. *Mol. Cell. Neurosci.* **50**, 35–44 (2012).
66. M. Fukuda, K. Mikoshiba, Doc2γ, a third isoform of double C2 protein, lacking calcium-dependent phospholipid binding activity. *Biochem. Biophys. Res. Commun.* **276**, 626–632 (2000).
67. A. Naito, S. Orita, A. Wanaka, T. Sasaki, G. Sakaguchi, M. Maeda, H. Igarashi, M. Tohyama, Y. Takai, Molecular cloning of mouse Doc2α and distribution of its mRNA in adult mouse brain. *Brain Res. Mol. Brain Res.* **44**, 198–204 (1997).
68. S. Orita, T. Sasaki, Y. Takai, Doc2 as a presynaptic modulator of Ca^{2+}-dependent neurotransmitter release. *Seikagaku* **71**, 530–535 (1999).
69. P. S. Kaeser, W. G. Regehr, Molecular mechanisms for synchronous, asynchronous, and spontaneous neurotransmitter release. *Annu. Rev. Physiol.* **76**, 333–363 (2014).
70. E. T. Kavalali, The mechanisms and functions of spontaneous neurotransmitter release. *Nat. Rev. Neurosci.* **16**, 5–16 (2015).
71. I. M. Yu, F. M. Hughson, Tethering factors as organizers of intracellular vesicular traffic. *Annu. Rev. Cell Dev. Biol.* **26**, 137–156 (2010).
72. D. J. James, T. F. J. Martin, CAPS and Munc13: CATCHRs that SNARE vesicles. *Front. Endocrinol. (Lausanne)* **4**, 187 (2013).
73. T. C. Südhof, The presynaptic active zone. *Neuron* **75**, 11–25 (2012).
74. H. Sakamoto, T. Ariyoshi, N. Kimpara, K. Sugao, I. Taiko, K. Takikawa, D. Asanuma, S. Namiki, K. Hirose, Synaptic weight set by Munc13-1 supramolecular assemblies. *Nat. Neurosci.* **21**, 41–49 (2018).
75. C. Ma, L. Su, A. B. Seven, Y. Xu, J. Rizo, Reconstitution of the vital functions of Munc18 and Munc13 in neurotransmitter release. *Science* **339**, 421–425 (2013).
76. M. Sato, Y. Mori, T. Matsui, R. Aoki, M. Oya, Y. Yanagihara, M. Fukuda, T. Tsuboi, Role of the polybasic sequence in the Doc2α C2B domain in dense-core vesicle exocytosis in PC12 cells. *J. Neurochem.* **114**, 171–181 (2010).
77. P. S. Pinheiro, H. de Wit, A. M. Walter, A. J. Groffen, M. Verhage, J. B. Sørensen, Doc2b synchronizes secretion from chromaffin cells by stimulating fast and inhibiting sustained release. *J. Neurosci.* **33**, 16459–16470 (2013).
78. S. C. Strickfaden, M. J. Winters, G. Ben-Ari, R. E. Lamson, M. Tyers, P. M. Pryciak, A mechanism for cell-cycle regulation of MAP kinase signaling in a yeast differentiation pathway. *Cell* **128**, 519–531 (2007).
79. S. M. Pearlman, Z. Serber, J. E. Ferrell Jr., A mechanism for the evolution of phosphorylation sites. *Cell* **147**, 934–946 (2011).
80. R. Friedrich, A. J. Groffen, E. Connell, J. R. van Weering, O. Gutman, Y. I. Henis, B. Davletov, U. Ashery, DOC2B acts as a calcium switch and enhances vesicle fusion. *J. Neurosci.* **28**, 6794–6806 (2008).
81. F. Nagano, S. Orita, T. Sasaki, A. Naito, G. Sakaguchi, M. Maeda, T. Watanabe, E. Kominami, Y. Uchiyama, Y. Takai, Interaction of Doc2 with tctex-1, a light chain of cytoplasmic dynein. Implication in dynein-dependent vesicle transport. *J. Biol. Chem.* **273**, 30065–30068 (1998).
82. R. V. Kalyana Sundaram, A. Chatterjee, M. Bera, K. Grushin, A. Panda, F. Li, J. Coleman, S. Lee, S. Ramakrishnan, A. M. Ernst, K. Gupta, J. E. Rothman, S. S. Krishnakumar, Roles for diacylglycerol in synaptic vesicle priming and release revealed by complete reconstitution of core protein machinery. *Proc. Natl. Acad. Sci. U.S.A.* **120**, e2309516120 (2023).
83. M. B. Dalva, M. A. Takasu, M. Z. Lin, S. M. Shamah, L. Hu, N. W. Gale, M. E. Greenberg, EphB receptors interact with NMDA receptors and regulate excitatory synapse formation. *Cell* **103**, 945–956 (2000).
84. J. T. Henderson, J. Georgiou, Z. Jia, J. Robertson, S. Elowe, J. C. Roder, T. Pawson, The receptor tyrosine kinase EphB2 regulates NMDA-dependent synaptic function. *Neuron* **32**, 1041–1056 (2001).
85. K. Hanamura, H. R. Washburn, S. I. Sheffler-Collins, N. L. Xia, N. Henderson, D. V. Tillu, S. Hassler, D. S. Spellman, G. Zhang, T. A. Neubert, T. J. Price, M. B. Dalva, Extracellular phosphorylation of a receptor tyrosine kinase controls synaptic localization of NMDA receptors and regulates pathological pain. *PLOS Biol.* **15**, e2002457 (2017).
86. C. C. Hoogenraad, A. D. Milstein, I. M. Ethell, M. Henkemeyer, M. Sheng, GRIP1 controls dendrite morphogenesis by regulating EphB receptor trafficking. *Nat. Neurosci.* **8**, 906–915 (2005).
87. N. K. Hussain, G. M. Thomas, J. Luo, R. L. Huganir, Regulation of AMPA receptor subunit GluA1 surface expression by PAK3 phosphorylation. *Proc. Natl. Acad. Sci. U.S.A.* **112**, E5883–E5890 (2015).
88. M. A. Takasu, M. B. Dalva, R. E. Zigmond, M. E. Greenberg, Modulation of NMDA receptor-dependent calcium influx and gene expression through EphB receptors. *Science* **295**, 491–495 (2002).
89. R. Janz, T. C. Südhof, R. E. Hammer, V. Unni, S. A. Siegelbaum, V. Y. Bolshakov, Essential roles in synaptic plasticity for synaptogyrin I and synaptophysin I. *Neuron* **24**, 687–700 (1999).

90. F. Onofri, M. Messa, V. Matafora, G. Bonanno, A. Corradi, A. Bachi, F. Valtorta, F. Benfenati, Synapsin phosphorylation by SRC tyrosine kinase enhances SRC activity in synaptic vesicles. *J. Biol. Chem.* **282**, 15754–15767 (2007).
91. M. Meijer, B. Dörr, H. C. Lammertse, C. Blithikioti, J. R. van Weering, R. F. Toonen, T. H. Söllner, M. Verhage, Tyrosine phosphorylation of Munc18-1 inhibits synaptic transmission by preventing SNARE assembly. *EMBO J.* **37**, 300–320 (2018).
92. M. Hruska, N. T. Henderson, N. L. Xia, S. J. Le Marchand, M. B. Dalva, Anchoring and synaptic stability of PSD-95 is driven by ephrin-B3. *Nat. Neurosci.* **18**, 1594–1605 (2015).
93. C. L. Essmann, E. Martinez, J. C. Geiger, M. Zimmer, M. H. Traut, V. Stein, R. Klein, A. Acker-Palmer, Serine phosphorylation of ephrinB2 regulates trafficking of synaptic AMPA receptors. *Nat. Neurosci.* **11**, 1035–1043 (2008).
94. A. H. Tang, H. Chen, T. P. Li, S. R. Metzbower, H. D. MacGillavry, T. A. Blanpied, A trans-synaptic nanocolumn aligns neurotransmitter release to receptors. *Nature* **536**, 210–214 (2016).
95. W. Jiang, R. Hua, M. Wei, C. Li, Z. Qiu, X. Yang, C. Zhang, An optimized method for high-titer lentivirus preparations without ultracentrifugation. *Sci. Rep.* **5**, 13875 (2015).

Acknowledgments: We thank C. Wang for providing the pCMV3-EphB2-Flag plasmid and fresh brain tissue samples of EphB2-deficient mice, X. Yang for providing the pFHUUIG_shortU6 (L309) plasmid, H. Zhang for support on NMR spectroscopy, and M. Zhang for insightful discussion. **Funding:** This work was supported by National Funds for Distinguished Young Scholars of China (32225024), National Science and Technology Major Project of China (2021ZD0202501), and National Natural Science Foundation of China (92254302, 32071224, and 31721002). **Author contributions:** C.M. conceived the experiments and supervised the study. H.Z., Y.Z., and S.X. generated all mutants and proteins used in this study. H.Z. performed most of in vitro experiments, and L.Z. and S.W. assisted with data analysis. M.L. and Y.Z. carried out in vivo electrophysiology experiments and analyzed the data. H.Z. and Y.Z. performed behavioral tests, and H.L., J.L., and Y. Lu assisted with data analysis. Z.H. and Y. Li performed the NMR experiments and analyzed the data. J.L. and Y. Lu provided helpful discussions and methodology. H.Z. and C.M. wrote the manuscript. **Competing interests:** The authors declare that they have no competing interests. **Data and materials availability:** All data needed to evaluate the conclusions in the paper are present in the paper and/or the Supplementary Materials.

Submitted 12 May 2023
Accepted 12 April 2024
Published 17 May 2024
10.1126/sciadv.adi7024